

Version1 – Photosynthesis Report

Photoproxy: Technical Assistance for the
Photosynthetic-Proxy Experiment

D1 of the Photoproxy campaign

27th of November 2019

Version 1

Issue 2 – Revision 1

Table of Contents

1	Introduction.....	5
1.1	Programmatic background of this activity	5
1.2	Scientific Introduction	6
1.3	Overview of objectives	7
1.4	Study sites.....	7
1.4.1	Selhausen, Germany.....	8
1.4.2	Majadas, Spain	8
1.4.3	Grosseto, Italy.....	9
1.4.4	Mead, United States.....	10
2	Material and Methods.....	12
2.1	Overview of measured data collected on the different study sites.....	13
2.1.1	Germany	13
2.1.2	Grosseto, Italy.....	15
2.1.3	Mead, USA.....	16
2.2	Data from other campaigns used in this study	17
2.2.1	Airborne imaging spectrometer <i>HyPlant</i> – Europe (FlexSense 2018).....	17
2.2.2	Airborne thermal sensor TASI - Europe (FlexSense 2018).....	18
2.3	Data specifically collected for Photoproxy.....	20
2.3.1	Airborne imaging spectrometer IBIS - University of Nebraska	20
2.3.2	Satellite-based data.....	23
2.3.3	Airborne carbon flux measurements.....	23
2.3.4	Ground-based high-performance point spectrometers for continuous measurements – FloX system.....	26
2.3.4.1	FloX located in Selhausen, Germany	26
2.3.4.2	FloX located in Lincoln, United States	33
2.3.4.3	FloX located in Majadas, Spain.....	33
2.3.4.4	FloX located in Grosseto, Italy.....	33
2.3.5	Ground based eddy covariance and ancillary measurements	33
2.3.6	Ground based vegetation measurements.....	34
2.4	Data processing	35
2.4.1	Calculation of vegetation products	35
2.4.1.1	Description of the used vegetation indices.....	35
2.4.1.2	Calculation of Vegetation Indices from FloX	37
2.4.1.3	Calculation of Vegetation Indices from <i>HyPlant</i>	40
2.4.1.4	Calculation of Vegetation Indices from satellite data	41
2.4.2	Calculation of Sun-Induced-Fluorescence Products.....	44

2.4.3	Calculation of GPP from continuous and stationary flux measurements	45
2.4.4	Calculation of carbon and water fluxes form airborne concentration measurements	45
3	Tentative Results and Discussion	47
3.1	Results from Selhausen, Germany	47
3.1.1	Seasonal dynamics of top-of-canopy measurements	47
3.1.2	Diurnal dynamics of top-of-canopy measurements.....	49
3.2	Results from Majadas, Spain	56
3.2.1	2018 Heatwave in Majadas, Spain	56
3.2.1.1	Seasonal dynamics.....	56
3.3	Results from Mead, USA.....	58
3.3.1	Seasonal dynamics.....	58
3.3.2	Diurnal dynamics	59
3.3.3	Aircraft SIF measurements	60
3.4	Results from Grosseto, Italy	61
3.5	Fluxes.....	62
4	Discussion	63
5	References.....	64
6	Acknowledgement.....	69

See tables with overflights/acquired data in the additional document: Supplemental Material.

Acronyms and Abbreviations

CCI	Chlorophyll Carotenoid index
EO	Earth Observation
ESA	European Space Agency
FLEX	FLuorescence EXplorer
FloX	FloX Box
FOV	Field of view
FWHM	Full Width at Half Maximum
FZJ	Forschungszentrum Jülich, Germany
GPP	Gross primary productivity
IOP	Intensive Observation Periods
LAI	Leaf area index
LWIR	Long wavelength infrared
NDVI	Normalized difference vegetation index
NIR	Near-infrared
NIRv	Near-infrared reflectance of terrestrial vegetation
SIF	Sun-induced fluorescence
SIF ₆₈₇	Intensity of Sun-Induced Fluorescence emitted at 687nm (red peak of fluorescence emission)
SIF ₇₄₀	Intensity of Sun-Induced Fluorescence emitted at 740nm (far-red peak of fluorescence emission)
SIF ₇₄₀	Intensity of Sun-Induced Fluorescence emitted at 760nm (fluorescence emission at O ₂ -A band)
SIF _{tot}	Intensity of total Sun-Induced Fluorescence emitted, integrated over the spectral window 679-780 nm
SNR	Signal to Noise ratio
SSI	Spectral Sampling Interval
SWIR	Short Wave Infrared
TIR	Thermal infrared
TOC	Top-of-canopy
VIS	Visible
VNIR	Visible and near-infrared

	Doc.: Photosynthesis report Version1		
	Date: 27.11.2019	Issue: 2	Revision: 1
	Ref.: ESA Contract No. ESA RFP/3-15506/18/NL/NF		Page: 5 / 69

1 Introduction

1.1 Programmatic background of this activity

In the framework of its Earth Observation Envelope Programme, the European Space Agency (ESA) carries out a number of different activities to support geophysical algorithm development, calibration, validation, and the simulation of future spaceborne earth observation missions.

The FLuorescence EXplorer (FLEX) will be the 8th Earth Explorer mission and will be the first mission designed to monitor the photosynthetic activity of terrestrial vegetation. Using a completely novel technique the chlorophyll fluorescence signal can be measured that originates from the core of the photosynthetic machinery. This will provide a completely new possibility to assess the dynamics of photosynthesis through sun-induced fluorescence, which offers a great advancement over current capabilities that can only detect potential photosynthesis derived from passive reflectance measurements by conventional land surface monitoring satellites. Sun-induced fluorescence can also be used to track transpiration.

Currently, various activities are ongoing to develop the scientific knowledge that is needed to prepare data products for the FLEX satellite mission and to prepare Cal / Val activities, which need to be in place at the time of the envisioned launch of the FLEX satellite in 2022.

This activity addresses relevant open aspects that are needed to develop the proposed level 2d data products of the FLEX satellite mission which are related to a quantitative assessment of vegetation photosynthesis and stress from space.

In few years from now, ESA's BIOMASS and FLEX Earth Explorers satellite missions will open a new opportunity to enhance our knowledge of the global carbon cycle. In particular, the scientific exploitation of BIOMASS and FLEX in synergy with the Sentinel satellite series and other existing and future missions (e.g. CMOS, GEDI, NISAR, Tandem-X/L) will provide an unprecedented opportunity to better understand and characterize the different components of the carbon cycle and its dynamics. Preparing for the fast exploitation of this unique and unprecedented observational capacity, ESA has launched the Carbon Science Constellation Initiative. This initiative will be implemented through a cluster of different studies, research activities, campaigns and tool development efforts dedicated to support the scientific community to explore the potential synergies between different Earth Observation approaches and maximize the scientific impact of this unique set of sensors for carbon cycle research.

Within the PhotoProxy project, we address relevant open aspects that are related to the quantitative assessment of vegetation photosynthesis and vegetation stress from space. In the past years the fluorescence signal that is emitted from the core of the photosynthetic apparatus during photosynthetic energy conversion, has become the most promising indicator of actual photosynthetic rates. In 2012, the European Space Agency has selected the FLEX satellite mission to become ESA's 8th Earth Explorer mission (Drusch et al. 2017). FLEX will be the first dedicated fluorescence mission that will provide global maps of both peak of the fluorescence signal on a high spatial resolution and relevant revisiting time.

In addition to fluorescence, which can be measured across various scales ranging from the single leaf to the ecosystem (Rascher et al 2015, Wieneke et al 2018), in recent years, alternative approaches to the remote detection of photosynthetic carbon fluxes (photosynthesis or gross primary productivity, GPP) have been proposed. These approaches include reflectance-based measures by NIRv (Badgely et al. 2017) and CCI (Gamon et al. 2016), which are both related to pigment and structurally-based changes in vegetation.

	Doc.: Photosynthesis report Version1		
	Date: 27.11.2019	Issue: 2	Revision: 1
	Ref.: ESA Contract No. ESA RFP/3-15506/18/NL/NF		Page: 6 / 69

Together, these remote sensing approaches offer a way to revolutionize our assessment of photosynthetic carbon uptake and vegetation health from space. However, major questions remain regarding the exact function of each of these signals and their relationship to each other. There are several indications that fluorescence may be the best remote sensing parameter to constrain predictions of CO₂ uptake rates, but we expect that a combination of the different measures will provide the best estimates of actual vegetation function.

1.2 Scientific Introduction

Land carbon sequestration plays a pivotal role in the global carbon cycle. Gross primary production (GPP) by plants is the major driver of land carbon sequestration. This process is directly linked to photosynthesis. A number of methods for assessing photosynthesis and GPP from satellite data have been proposed over the years. These include the light-use efficiency model based on reflectance indices and upscaling methods using machine-learning approaches applied to flux tower and satellite data from Sentinel 2 and 3. However, key limitations of these reflectance-based methods have been identified including the fact that multiple factors (besides photosynthesis or GPP) influence the reflectance signals (over-determination). Additionally, these estimates are often based on timely and spatially integrated data and therefore reflect only seasonal patterns on ecosystem scales. For this reason, reflectance-based indices cannot represent rapid changes in photosynthesis.

Sun-induced chlorophyll fluorescence (SIF) has evolved as an alternative method for assessing photosynthesis and GPP, based on new satellites (Joiner et al. 2011, Frankenberg et al. 2011). SIF signal is emitted from the core of the photosynthetic apparatus during photosynthetic energy conversion, has become the most promising indicator of actual photosynthetic rates. The red and far-red fluorescence signal (F687 and F760) are closely related to the amount and the efficiency with which light energy is used in the first steps of photosynthesis (the so-called 'light reactions'). Most of the SIF-based approaches from satellites have been applied over large spatial and temporal scales. This integration was necessary to be able to retrieve the relatively small signal from such a huge distance through the atmosphere. However, this integration over time and space obscures the mechanistic underpinnings.

Future FLuorescence EXplorer (FLEX) satellite missions will provide for the first time global maps of both peak of the fluorescence signal on a high spatial resolution and relevant revisiting time. This mission is part of ESA's Carbon Science constellation Initiative which aims to frame all activities ongoing for a better understanding of global carbon cycle. Due to the high-resolution spectrometer on board and using a completely novel technique the chlorophyll fluorescence signal can be measured that originates from the core of the photosynthetic machinery. This will provide a completely new possibility to assess the dynamics of photosynthesis through sun-induced fluorescence, which offers a great advancement over current capabilities that can only detect potential photosynthesis derived from passive reflectance measurements by conventional land surface monitoring satellites. Sun-induced fluorescence can also be used to track transpiration.

While these fluorescence-based approaches offer improvements over reflectance-based approaches, key questions remain. In particular, the degree to which structural and physiological factors influence the SIF signal, the degree to which these effects vary at shorter time scales, and the degree to which vegetation type (e.g. functionally different ecosystems having different biomass) affect the SIF signal (e.g. Guanter et al. 2012).

In addition to fluorescence, which can be measured across various scales ranging from the single leaf to the ecosystem (Rascher et al 2015, Wieneke et al 2018), in recent years, alternative approaches to the remote detection of photosynthetic carbon fluxes (photosynthesis or gross primary productivity,

	Doc.: Photosynthesis report Version1		
	Date: 27.11.2019	Issue: 2	Revision: 1
	Ref.: ESA Contract No. ESA RFP/3-15506/18/NL/NF		Page: 7 / 69

GPP) have been proposed. These approaches include reflectance-based measures by NIRv (Badgely et al. 2017) and CCI (Gamon et al. 2016), which are both related to pigment and structurally-based changes in vegetation. This studies suggest that over certain time scales and for certain vegetation types, there is a close correlation between reflectance-based pigment signals (e.g. CCI) and fluorescence-based approaches (Springer et al. 2017).

Together, these remote sensing approaches offer a way to revolutionize our assessment of photosynthetic carbon uptake and vegetation health from leaf up to space level. However, all named RS parameters (NDVI, EVI, SIF, CCI, and NIRv) are typically developed for a certain spatial scale and therefore are not directly transferable to other spatial scales. Therefore, major questions remain regarding the exact function of each of these signals, their relationship to each other, and the best way to integrate them. There are several indications that fluorescence may be the best remote sensing parameter to constrain predictions of GPP (CO₂ uptake) rates. However, it is likely that combining fluorescence metrics with reflectance indices can enhance our understanding of photosynthesis beyond what is possible from fluorescence alone. Currently, there is no comprehensive study available that investigates the power and transferability of these combined remote sensing parameters.

1.3 Overview of objectives

There are several indications that fluorescence may be the best remote sensing parameter to constrain predictions of CO₂ uptake rates, but we expect that a combination of the different measures will provide the best estimates of actual vegetation function. Thus, a key hypothesis to be tested is that reflectance-based and fluorescence-based metrics in combination offer a superior approach to photosynthesis and GPP assessment.

With this activity, we aim to address the following objectives:

1. Test the applicability of the recently developed reflectance indices CCI and NIRv to track diurnal and seasonal vegetation dynamics.
2. Perform a comparison of CCI, NIRv and sun induced chlorophyll fluorescence (SIF) to better judge the quality of the different approaches to understand and model vegetation dynamics.
3. Compare a benchmark dataset of those parameters to flux estimates from airborne and ground based systems.
4. Determine the scale-dependence (temporal and spatial) of the correlation between each optical metric and photosynthesis or GPP.
5. Determine the factors that confound the interpretation of (fluorescence and) reflectance based signals, and the conditions under which these occur.
6. Determine the degree by which physiological regulation and structural adjustments influence each signal.

1.4 Study sites

During the 2018 FLEXsense campaign real-measured data covering ground, airborne and satellite scale on different sites over the globe have been collected for the first time. In this study, we make use of this unique dataset in combination with local flux measurements to derive optical RS parameters and GPP. These combined measurement of pigments, canopy structure, fluorescence, and gas fluxes will be key to addressing the above described objectives.

1.4.1 Selhausen, Germany

The highly instrumented long-term observation site was established in the years 2006 by the German Science Foundation (DFG), the University of Köln, the University of Bonn, and Forschungszentrum Jülich (FZJ). National funding, such as the TERENO network of the Helmholtz Association and the 12 year funding of the DFG funded Transregio TR32, ensures the long-term operation of the site's instruments. The site covers an area of approximately 100 x 40 km and can be described as an anthropogenically influenced area consisting of different ecosystems that includes intensive agricultural fields, managed pine and mixed forest, natural grasslands, and swamp areas. The catchment of the Rur covers 2354 km² and is mainly situated in Western Germany with about 157 km² (6.7 %) extending into Belgium and about 108 km² (4.6 %) into the Netherlands (Figure 1). Further information can be found at <http://tr32new.uni-koeln.de/> and in Simmer et al (2015). The site is mainly equipped with a dense network of nationally funded meteorological measurement stations complemented by several eddy flux towers. Additionally, since 2012, the *HyPlant* sensor has mapped a core region (app. 15 x 10 km) every year. Various ground measurements of sun-induced fluorescence, eddy covariance, and various vegetation parameters complements this time series of maps.

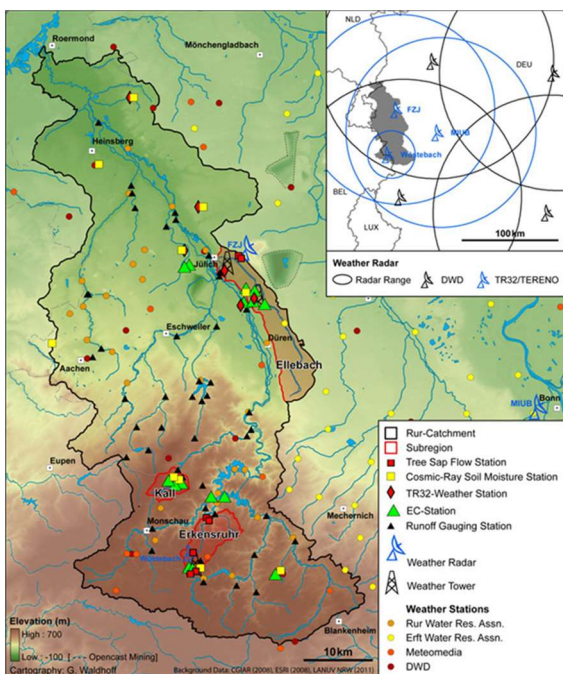


Figure 1: Overview of the Transregio intensive study site that is equipped with an extraordinary dense network of ground and atmospheric measurement systems. The site is a catchment and covers several vegetation areas.

1.4.2 Majadas, Spain

The ecosystem is a typical 'Iberic Dehesa', with an herbaceous stratum of native pasture and a tree layer of scattered oak trees, with 98 % of the trees being *Quercus ilex*. The tree density is about 20 - 25 trees ha⁻¹ with a mean DBH of 46 cm and a canopy height of about 8 m. The canopy fraction of the trees is about 20 %. The herbaceous layer consists mostly of various annual native species such as *Vulpia bromoides* (L.), *Vulpia geniculata* (L.), *Trifolium subterraneum* (L.) and *Ornithopus compressus* (L.) with often more than 20 species within 4 m². The fractional cover of the three main functional plant forms within the pasture (grasses, forbs and legumes), varies spatially but also seasonally according to their phenological status (Perez-Priego et al., 2015). The LAI of the trees is around 0.35 m² m⁻² (1.5 - 2.0 m² m⁻² on a tree basis) while the spring peak green LAI of the herbaceous layer ranges between 2 - 4 m² m⁻² depending on the season.

The savanna is managed and used for continuous grazing of extensive livestock with a low density of 0.3 cows ha⁻¹. During the driest summer months (July - September) most of the cattle are usually moved to nearby mountain grasslands. Mean annual temperature is 16.7 °C and annual precipitation is ca. 650 mm with large inter-annual variability. The prevailing wind directions are West-Southwest and East-Northeast.

Table 1: Coordinates of eddy flux towers at the Majadas site.

Site code	PI	Lat	Lon
CT (Control Tower)	CEAM Arnaud Carrara	39°56'25.12"N	5°46'28.70"W
FLUXNET 'ES-Lma'			
NT (Nitrogen Addition Tower)	MPI-BGC Mirco Migliavacca	39°56'33.68"N	5°46'43.26"W
FLUXNET 'ES-Lm1'			
NPT (Nitrogen Phosphorous Tower)	MPI-BGC Mirco Migliavacca	39°56'4.53"N	5°46'33.17" W
FLUXNET 'ES-Lm1'			
SMANIE	MPI-BGC Mirco Migliavacca	39°56'24.68" N,	5°45'50.27"W

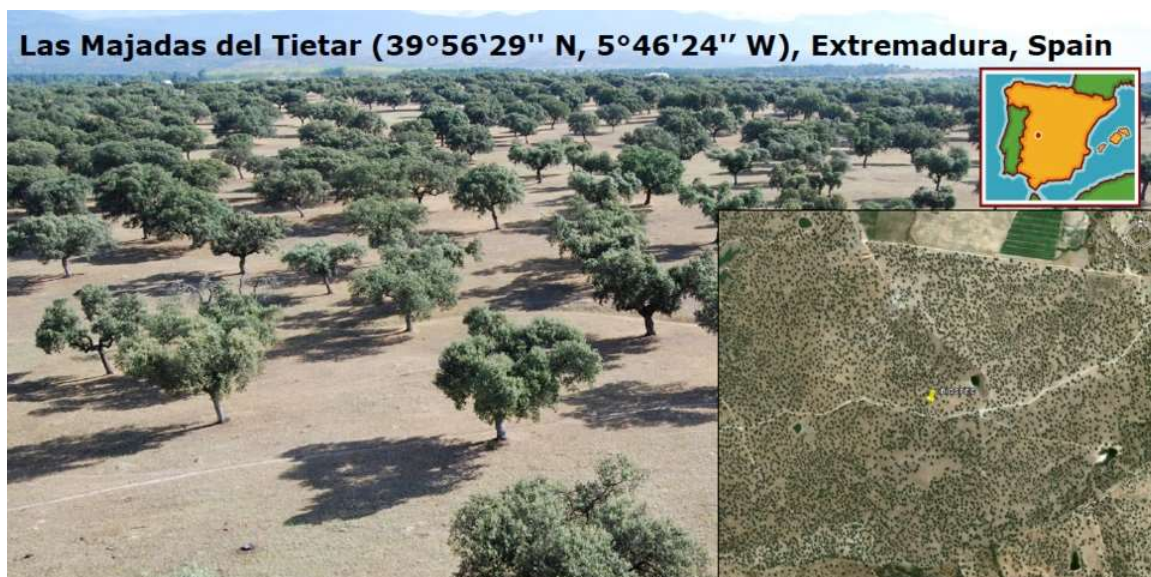


Figure 2: Image from the top of the eddy covariance tower of the experimental site in Majadas de Tietar (Spain). Photo by Dr Arnaud Carrara (CEAM).

1.4.3 Grosseto, Italy

This experimental site is located in central Italy at 20 km from the coastline in central Tuscany (Figure 3). The site is part of a milk production farm. It mainly consists of a large irrigated flat area extending over 72 ha. The area has a circular shape with 1 km diameter and is irrigated by a rotating pivot-irrigation system, which is normally operated 24h a day in the period June-August. A full irrigation cycle is completed within 4 days. The area was cultivated with a grass mixture from January to May 2018 and then entirely planted with corn at the end of May. This crop was grown during the period June - September under full irrigation and fertilization reaching full canopy cover at mid / end July and

	Doc.: Photosynthesis report Version1		
	Date: 27.11.2019	Issue: 2	Revision: 1
	Ref.: ESA Contract No. ESA RFP/3-15506/18/NL/NF	Page: 10 / 69	

a maximum height of 2.8 / 3.0 m in mid-August. From June onwards the area was surrounded by dry grasslands / soils where no ETP is expected to occur.



Figure 3: Le Rogaié field site.

1.4.4 Mead, United States

Mead, Nebraska, is an agricultural site located in the heart of the maize and soybean cultivation region of the US Midwest, one of the hotspots of the global SIF signal. Crops are typically maize and soybeans rotations (planted in alternate years), and may be irrigated or rain-fed.

Below (Figure 5) is a set of images of the key Mead sites, which contain plots of maize and soybean (CSP 1-3) among other sites. Aircraft imagery (starting in 2017) includes spectral reflectance (AISA Kestrel, Specim), and fluorescence (IBIS, Specim). These sites were flown in 2018 coincident with the Sentinel-3B overpass, under mostly sunny skies. Crops are maize and soybeans, including irrigated and rain-fed plots, and other crops, pastures, and forest shelterbelts are in the vicinity. All three sites are core Ameriflux sites (NE1-NE3).

Mead (Nebraska) Flux Tower Coordinates:

NE3 (CSP3): 41.1796700, -96.4396500 (this is the primary site with the D-FloX)

NE2 (CSP2): 41.1648700, -96.4701

NE1 (CSP1): 41.1650600, -96.4766400



Figure 4: Mounting of D-FloX and other SIF sensors.

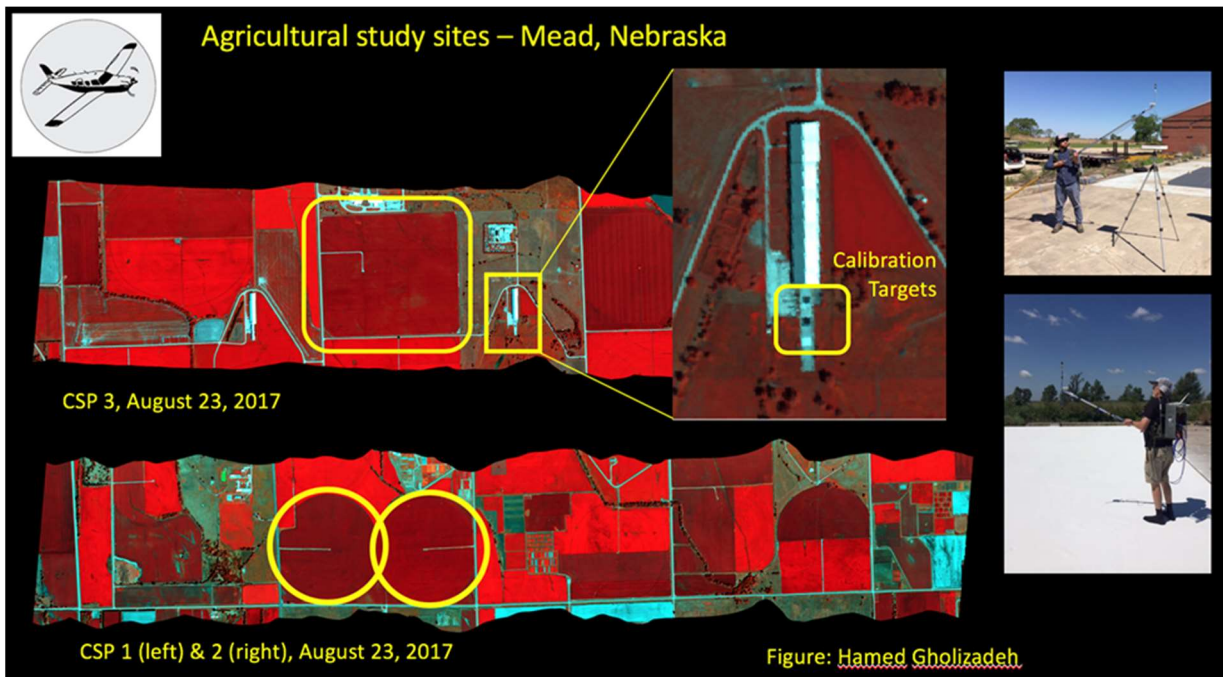


Figure 5: Field sites (CSP 1, 2, & 3) at Mead, Nebraska, 23th August, 2017, shown in false-color IR images taken from the AISA Kestrel. Images corrected to surface reflectance using ground calibration targets (right) and the empirical line correction method.

	Doc.: Photosynthesis report Version1		
	Date: 27.11.2019	Issue: 2	Revision: 1
	Ref.: ESA Contract No. ESA RFP/3-15506/18/NL/NF		Page: 12 / 69

2 Material and Methods

The material and method part is divided into two chapters. In the first chapter, we describe existing data from other campaigns that we use for our analysis (e.g. AtmoFlex, FlexSense). In the second chapter, we describe specific measurements that we use to understand the entire pipeline from leaf to satellite in different contrasting ecosystems.

Data from Sentinel-2 are included in the Supplemental material-1, while the overview over *HyPlant* data are summarized in Supplemental material-2.

2.1 Overview of measured data collected on the different study sites

2.1.1 Germany

Table 2: Overview of satellite, airborne and ground-based measurements for the entire observable time period in the Photoproxy campaign in Selhausen, Germany. SIFSys Box4 was installed on winter wheat field (50.590° N, 8.533° E) and FloX JB-011-JF was installed on winter wheat field (50.589775° N, 8.532838°E). S: Sentinel.

DATE	Satellite		Airborne HyPlant	Canopy and leaf level			Vegetation parameters		Ecosystem GPP	Cloud coverage
	S-3A reprogram.	S-3B		SIFSys Box-4	FloX JB-011-JF	SunScan	Destructive GAI biomass	Non-destructive plant height		
01.04.2018										
02.04.2018				Y					Y	
03.04.2018										
04.04.2018				Y				Y	Y	
05.04.2018										
-				Y					Y	
08.04.2018										
09.04.2018				Y				Y	Y	
10.04.2018										
-				Y					Y	
16.04.2018										
17.04.2018				Y				Y	Y	
18.04.2018				Y					Y	
19.04.2018				Y					Y	
20.04.2018				Y		Y			Y	
21.04.2018										
-				Y					Y	
24.04.2018										
25.04.2018				Y				Y	Y	
26.04.2018										
27.04.2018				Y					Y	
28.04.2018										
29.04.2018									Y	
30.04.2018									Y	
01.05.2018									Y	
02.05.2018								Y	Y	
03.05.2018										
04.05.2018									Y	
05.05.2018										
06.05.2018									Y	
07.05.2018					Y				Y	
08.05.2018					Y				Y	
09.05.2018					Y			Y	Y	
10.05.2018					Y				Y	
11.05.2018					Y				Y	
12.05.2018				Y	Y				Y	
13.05.2018				Y	Y				Y	
14.05.2018				Y	Y			Y	Y	
15.05.2018				Y	Y			Y	Y	
16.05.2018				Y	Y				Y	
17.05.2018				Y	Y				Y	
18.05.2018				Y	Y	Y	Y	Y	Y	
19.05.2018				Y	Y				Y	
20.05.2018				Y	Y				Y	
21.05.2018				Y	Y				Y	
22.05.2018				Y	Y			Y	Y	
23.05.2018										
-				Y	Y				Y	
27.05.2018										
28.05.2018				Y	Y			Y	Y	
29.05.2018										
-				Y	Y				Y	
03.06.2018										
04.06.2018				Y				Y	Y	partly cloudy
05.06.2018				Y					Y	cloudy
06.06.2018				Y					Y	
07.06.2018				Y					Y	
08.06.2018				Y					Y	

09.06.2018						Y
13.06.2018						
14.06.2018		Y		Y		Y
15.06.2018						
16.06.2018		Y				Y
17.06.2018						
18.06.2018		Y	Y	Y		Y
19.06.2018		Y				Y
24.06.2018						
25.06.2018		Y		Y		Y
26.06.2018		2 overflights	Y			Y
27.06.2018		1 overflight	Y			Y
28.06.2018	Y		Y			Y
29.06.2018		3 overflights	Y			Y
30.06.2018			Y			Y
01.07.2018			Y			Y
02.07.2018	Y		Y	Y		Y
03.07.2018						
04.07.2018		Y				Y
05.07.2018						
06.07.2018		Y				Y
07.07.2018		Y				Y
08.07.2018		Y				Y
09.07.2018		Y		Y		Y
10.07.2018			Y			
15.07.2018		Y				Y
16.07.2018		Y		Y		Y
17.07.2018		Y				Y
18.07.2018		Y				Y
19.07.2018		Y				Y

clouds before noon
no clouds

no clouds

no clouds

2.1.2 Grosseto, Italy

Table 3: Overview of satellite, airborne and ground-based measurements for the entire observable time period in the Photoproxy campaign in Grosseto, Italy. S: Sentinel.

DATE	Satellite			MODIS S-5P	Airborne		Canopy and leaf level			Vegetation parameters			Ecosystem	Ecosystem	Cloud coverage
	S-3A	S-3B	S-2		HyPlant	Fluxes Metair (Measurements Duration)	FLOX JB-009-ESA	Destr.	Non-destr.	GPP	GPP				
	reprogram.											Lat.	Lon.	Crop	
10.06.2018				Y	Y (18 overpasses at 680m, 4 at 3050m)		42,828	11,076	ALFAALFA				Y	Y	OK, no clouds
14.06.2018	Y			Y	Y (5 overpasses)		42,828	11,076	ALFAALFA				Y	Y	
16.06.2018				Y	Y (3 overpasses)		42,828	11,076	ALFAALFA				Y	Y	
19.06.2018					Y (6 overpasses)	Y (3h 44min)	42,828	11,076	ALFAALFA				Y	Y	OK, no clouds
21.06.2018	Y				Y (5 overpasses)	Y (3h 57min)	42,828	11,076	ALFAALFA				Y	Y	
03.07.2018	Y		Y	Y		Y (3h 51min)	42,828	11,076	ALFAALFA				Y	Y	
07.07.2018	Y			Y	Y (4 overpasses)		42,828	11,076	ALFAALFA				Y	Y	clouds and cloud shadows in all overpasses
18.07.2018	Y		Y		Y (40 overpasses)	Y (3h 19min)	42,826	11,069	CORN				Y	Y	Small clouds in the afternoon (after 14 PM local time)
20.07.2018				Y	Y (28 overpasses)	Y (4h 14min)	42,826	11,069	CORN				Y	Y	clouds only in the flightline at 14 06 LOCAL time
30.07.2018	Y			Y	Y (6 overpasses)		42,826	11,069	CORN				N	N	Some small clouds in 2 of the overpasses
31.07.2018				Y	Y (4 overpasses)		42,826	11,069	CORN				Y	Y	

2.1.3 Mead, USA

Table 4: Overview of satellite, airborne and ground-based measurements for the entire observable time period in the Photoproxy campaign in Mead, USA. Processed data will be subjected to reprocessing for consistency. LI-6400 (gas exchange) from Tom Avenson (LI-COR). Date are shown for CSP3 (rainfed maize). S: Sentinel.

DATE	Satellite		Airborne		Canopy and leaf level			Vegetation parameters		Ecosystem GPP	Note	DATE (DOY)
	Sentinel 3A	Sentinel 3B reprogram.	Kestrel	IBIS	D-Flox Diurnal	Licor light bars (LAI)	Licor6800 leaf gas exchange	Destructive GAI	Non-destructive biomass plant height m			
26.05.2018					processed	available				processed		146
-												-
27.06.2018					processed	available				processed		178
28.06.2018			(processed)	(processed)	processed	available				processed		179
29.06.2018					processed	available				processed		180
-												-
08.07.2018					processed	available				processed		189
09.07.2018				(processed)	processed	available				processed		190
10.07.2018					processed	available				processed		191
-												-
20.07.2018					processed	available	available			processed		201
21.07.2018		available	(processed)*	(processed)*	processed	available				processed	*3 flights	202
22.07.2018					processed	available				processed		203
-												-
01.08.2018					processed	available				processed		213
02.08.2018		available	(processed)*	(processed)**	processed	available				processed	**2 flights	214
03.08.2018					processed	available				processed		215
-												-
16.08.2018					processed	available				processed		228
17.08.2018					processed	available	available			processed		229
18.08.2018					processed	available				processed		230
-												-
23.08.2018					processed	available				processed		235
24.08.2018			not processe	(processed)	processed	available				processed		236
25.08.2018					processed	available				processed		237
-												-
16.09.2018					processed	available				processed		259
17.09.2018			(processed)	(processed)	processed	available				processed		260
18.09.2018					processed	available				processed		261
-												-
15.10.2018					processed	available				processed		288
16.10.2018			(processed)	(processed)	processed	available				processed		289

2.2 Data from other campaigns used in this study

2.2.1 Airborne imaging spectrometer *HyPlant* – Europe (FlexSense 2018)

The *HyPlant* sensor is a hyperspectral imaging system for airborne and ground-based use. It consists of two sensor heads. The DUAL module is a line-imaging push-broom hyperspectral sensor, which provides contiguous spectral information from 370 to 2500 nm in one device utilizing a common fore objective lens with 3 nm spectral resolution in the VIS / NIR spectral range and 10 nm spectral resolution in the SWIR spectral range. The vegetation fluorescence signal is measured with a separate push-broom sensor, the FLUO module, which produces data at high spectral resolution (0.25 nm) in the spectral region of the two oxygen absorption bands. The data acquisition and power unit contain two rack modules. The first module includes the data acquisition computer with system control and data acquisition software. Furthermore, it contains the power supply and the control electronics for the DUAL module and GPS/INS sensor. The second module includes the same equipment for the FLUO module. The position and altitude sensor (GPS/INS sensor) provides, synchronously with the image data, aircraft position and altitude data for image rectification and geo-referencing. Both imagers (DUAL and FLUO module) are mounted in a single platform with the mechanical capability to align the field of view (FOV) (Figure 6).

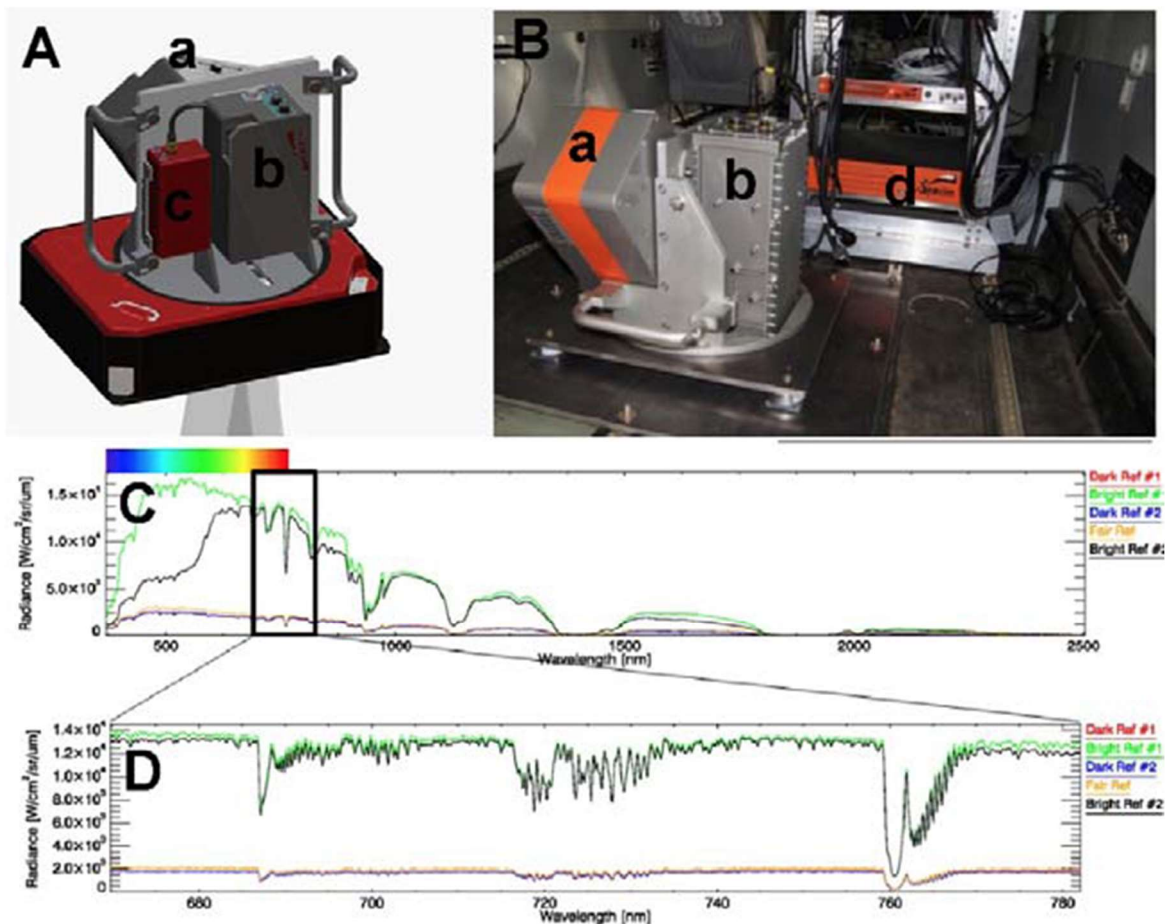


Figure 6: Schematic drawing of the *HyPlant* sensor consisting of the broad band dual module (a) and the high resolution fluorescence module (b). Additionally, the GPS / IMU positioning unit that is attached to the rack is shown (c). B: Installation of *HyPlant* within a Cessna aircraft. In the back, the data acquisition unit is visible (d) C, D: Representative radiance measurements from different surfaces from the DUAL and the FLUO module, respectively.

Table 5 shows the radiometric performance of the airborne sensor *HyPlant*. The values were obtained during the technical evaluation of the sensor and are published in Rascher et al. (2015). *HyPlant* imaging spectrometer was specifically designed for vegetation monitoring and to retrieve sun-induced fluorescence (and concurrent reflectance). *HyPlant* consists of two modules: (i) the broad band dual-channel module to measure surface reflectance in the visible and near-infrared spectral region (380 – 2500 nm) and (ii) the fluorescence module having a high spectral resolution in the red spectral range (670-780 nm) that is designed for fluorescence retrievals. Performance characteristics given in this table were performed on flight data using several flight lines and a forward modelling of atmospheric absorption characteristics. Signal-to-noise ratios (SNR) (data in brackets) are calculated from laboratory measurements.

Performance characteristics of <i>HyPlant</i>			
Sensor	Dual-Channel Module		Fluorescence Module
<u><i>Spectral performance</i></u>			
Wavelength range [nm]	380 – 970	970 – 2500	670 – 780
Bands	p350	272	1024
Wavelength sampling interval [nm]	1.7	5.5	0.11
Wavelength resolution (FWHM) [nm]	4.0	13.3	0.25 at O ₂ -A 0.23 at O ₂ -B
Band broadening [nm]	0.2	0.2	0.01 at O ₂ -A 0.03 at O ₂ -B
Spectral shift [nm]	1.2	2.4	< 0.04
Smile [nm]	0.4	1.2	< 0.01 at O ₂ -A 0.01 at O ₂ -B
<u><i>Radiometric performance</i></u>			
SNR with full scale signal	(510)	(1100)	(240)
Stay light and pixel cross talk [%]			< 0.5
<u><i>Spatial performance</i></u>			
Spatial pixels	384	384	384
Field of view [°]	32.3		32.3
Instantaneous Field of view [°]	0.0832		0.0832
Swath [m]	380 at 600 m agl ¹ 1140 at 1780 m agl		380 at 600 m agl 1140 at 1780 m agl
Spatial sampling interval (across track) [m]	0.98 at 600 m agl 2.94 at 1780 m agl		0.98 at 600 m agl 2.94 at 1780 m agl
Keystone [µm]			
<u><i>Sensor type</i></u>			
Type	CMOS	MCT	sCMOS ²
Dynamic range [bit]	12	14	16

¹agl: above ground level

²sCMOS: ‘scientific CMOS’ chip. A new CCD chip technology that combines different enhancements to achieve high light sensitivity with linear sensitivity.

2.2.2 Airborne thermal sensor TASI - Europe (FlexSense 2018)

TASI-600 is a push-broom hyperspectral thermal sensor system designed specifically for airborne use by the Canadian company Itres. The TASI is sensitive to wavelengths in the Long Wave Infrared (LWIR) part of the electromagnetic spectrum. This instrument measures the intensity of emitted radiance

from the imaged target across 32 spectral bands in the range of 8 to 11.5 microns. The TASI-600 collects an image swath of 600 pixels ‘across track’ by 1 pixel ‘along track’. The raw imagery from the TASI has a data depth of 14-bits (0 - 16,383). The in this study used TASI is equipped by on-board dual black body calibration, which enable to perform radiometric calibration for each flight line during flight and improve radiometric accuracy. As thermal sensor, TASI could be used for a number of applications i.e. forest or agriculture ecosystem monitoring as well as for archaeological or urban heat islands detection. Basic technical specifications of the TASI hyperspectral system are shown in Table 6.

Table 6: TASI-600 specifications

Sensor	TASI-600
Spectral Region	LWIR
Sensor Type	Push-broom Hyperspectral TIR
Spectral Bands	32
Spectral Range [nm]	8 000 – 11 500
Number of Spatial Pixels	600
Max. Spectral Resolution [nm]	110
FOV [°]	40
IFOV [°]	0.07
Dynamic Range	14-bits (16384:1)
Burst Data Rate	5 Mpix/sec
NEDT	TASI-600/32: 0.11° C @ 100° C
Spectral Smile	TASI-600/32: < ±0.25 pixels
Keystone Distortion	TASI-600/32: < ±0.25 pixels



Figure 7: TASI-600 and laser scanner (LiDAR) Riegl LMS-Q780 mounted in the aircraft together with HyPlant.

2.3 Data specifically collected for Photoproxy

2.3.1 Airborne imaging spectrometer IBIS - University of Nebraska

The University of Nebraska's CHAMP (CALMIT Hyperspectral Airborne Monitoring Program) flies an instrument combination similar to that of the *HyPlant* sensor in that it combines a vis-NIR imaging spectrometer (AISA Kestrel 10, Specim) with a fluorescence imager (AISA IBIS, Specim) (Table 7 and 8). This system was operated on several times during the 2018 vegetation period covering the Mead study sites (Table 9)

Table 7: Specifications of the airborne imaging spectrometer IBIS.

AISA-IBIS Specifications	
Spectral range	670-780 nm
Spectral sampling	0.11/0.22 nm
F/#	F/1.7
Signal-to-noise ratio (peak)	680:1
Spatial pixels	384/768
Frame rate	Up to 65 Hz
Integration time	Adjustable, within frame time
FOV, focusing range	32.3 deg., 0.5m to ∞
Electro-mechanical shutter	Yes
Optics temperature stabilization	Yes
Detector	sCMOS, snapshot mode
Detector cooling	Peltier
Data interface	CameraLink 16-bit
Power consumption	Nominal 135W, Max 200W
Input voltage	18-36 VDC
Mechanical Characteristics	
Sensor Size	588 x 227 x 160 mm
DPU size	300 x 260 x 195 mm
Sensor weight	14.2 kg
DPU weight	9.5 kg
Environmental Characteristics	
Storage temperature	-20 to +50 deg. C
Operating temperature	+5 to +30 deg. C, non-condensing

Table 8: Specifications of the AISA-Kestrel 10.

AISA-Kestrel 10 Specifications

Camera specifications

Spectral range	400-1000 nm
Spectral sampling	1.75/3.5/7 nm
F/8	F/2.4
Smile/Keystone	<0.5 pixels
Polarization sensitivity	< ± 2%
Signal-to-noise ratio (peak)	400-800
Spatial resolution	2040 pixels
Frame rate	Up to 170 or 100 Hz
Integration time	Adjustable within frame period
FOV	40 degrees
Electro-mechanical shutter	Yes
Data interface	CameraLink 12-bit
Data storage	480 Gb SSD
Total system power, (GNSS/IMU, DPU)	<41W

Mechanical characteristics (unmounted)

Camera dimensions (weight)	127 x 180 x 225 mm (2.1 kg with front lens)
DPU dimensions (weight)	165 x 154 x 101 mm (1.6 kg)
GNSS/IMU dimensions (weight)	120 x 70 x 40 mm (0.5 kg)
Total systems weight	4.75 kg

Environmental characteristics

Storage temperature	-5 to +50 degrees C
Operating temperature	+5 to +40 degrees C, non-condensing

Table 9: Dates of the measurements with IBIS in Mead, USA.

Notes		Sites							Legend	
DOY	Date	9-Mile Prairie	CSP 1&2	CSP 3	CSP 4	CSP NS	LTAR 1	LTAR 2 (& CITB)	Data available	No data
Due to issues with the GPS onboard, some images on June 28 are not correctly georeferenced	179	20180628								
	202	20180721_AM								
	202	20180721_Noon								
Cloudy	202	20180721_PM (cloudy)								
	214	20180802_Noon								
No target scans for this date. Used the scans from 20180802 PM.	214	20180802_PM								
	236	20180824								
	260	20180917								
	289	20181016								

For more information on the files, check out file header.

for details: Hamed Gholizadeh
 (hamed.gholizadeh@unl.edu;
 h.gholizadeh1@gmail.com)

CSP 1-4 and LTAR 2: sites with an eddy covariance towers

CSP-3: primary site with D-FloX

2.3.2 Satellite-based data

The tables 1 – 4 in the Supplemental material-1 give an overview on the Sentinel-2 data that were acquired under cloud free conditions from June 1st until August 31st 2018 of the field sites in Grosseto, Italy, Selhausen, Germany, Majadas, Spain and Mead, USA.

Raw observations may include cloud / snow covered pixels that need to be filtered out before using them in any following analyses. For each observation, there is a scene classification layer (*.SCL*.tif) that can be used for filtering low quality (or undesired) pixels. The SCL layer is only available at two resolutions: 20 m and 60 m. To filter out 10 m bands, a resampling of the 20 m SCL layer can be taken (suggested resampling method: Nearest Neighbour). If a pixel is undesired (as indicated “mask out”), it can be excluded by assigning NA value by the users.

For a detailed view of the available data, please see the supplemental material. Here, we refer to the Sentinel-2 and Sentinel-3 data base, which we developed during the FlexSense 2018 study.

2.3.3 Airborne carbon flux measurements

For the airborne carbon flux measurements a research aircraft of MetAir (Switzerland) was employed over Italy. The aircraft is equipped with two underwing pods that are equipped with atmospheric measurement instruments, which are well exposed to undisturbed air. Each pod has its own computer, communicating with the main pc in the baggage compartment via bluetooth.

In the present configuration for this campaign, the left-hand-pod was almost empty, only equipped with an optical aerosol counter, a laser altimeter [100 Hz, 0.2 m precision, 1 m accuracy] and a vertical camera [remotely controlled by the operator]. The right-hand-pod contained the system for measuring wind (five-hole probe, accelerometers and a high-grade IMU), a fast thermometer (10 Hz), a dew-point mirror and two IR-absorption instruments (modified LI-6262 and LI-7500) for H₂O, and the same two modified LiCor's for CO₂. The modified LI-6262 is equipped with a reference gas of known concentration (380 ppm CO₂). This LI-6262 has a very high accuracy (0.4 ppm), but a slow measurement frequency (about 0.1 Hz), whereas the LI-7500 is measuring fast, but not very accurately and can drift easily by several ppm due to varying aerosols. In the post-processing, the two instruments are combined in order to achieve both a high accuracy and precision at the high temporal resolution. Measurements of the vertical wind and the concentrations of CO₂ and H₂O are executed. The measurements are done at high temporal resolution (10 Hz) as close to the surface as possible.

These combined atmospheric measurements of concentrations can then be converted in flux measurements taken various assumptions into account. There are five main factors influencing the reliability of such airborne vertical flux measurements:

- i) High precision of the measurements at 10 Hz
- ii) Sufficient accuracy for getting meaningful averages also for long-wave contributions
- iii) Suitable meteorological conditions (depending from iv as well)
- iv) Possibility for flying as low as 50 m agl. (reason explained below)
- v) Suitable flight pattern over the surface type under study

Since at higher distance from the surface, additional factors can influence the measurements, the aircraft is flying as low as possible. If the flight have be executed at higher altitudes, measurements are only possible at weak wind (< 5 m/s or 10 kt). In principle, the total flux is given by the mean advective fluxes and the turbulent fluxes for all three dimensions: vertical, lateral, longitudinal. With a low distance between the surface and the height of the measurements, the three dimensions can interact,

	Doc.: Photosynthesis report Version1		
	Date: 27.11.2019	Issue: 2	Revision: 1
	Ref.: ESA Contract No. ESA RFP/3-15506/18/NL/NF		Page: 24 / 69

i.e. a horizontal advective flux from a neighbouring surface type can influence the vertical flux over the surface below the flight track. Further, waves in the atmosphere can lead to artefacts. Flight tracks along such waves (small angle between the wave crests and the track) can produce strong artefacts. The same is true for terrain induced flows, which needs to be considered in the post-processing.

Table 10: DIMO HB-2335 technical specifications and scientific instruments on board the aircraft.

Type of aircraft	TMG (Touring Motor Glider) - DIMO HK36 TTC-ECO (two seated single engine piston aircraft with long endurance and good aerodynamic performance, with 16.5 m wing span)
Manufacturer	Diamond Aircraft, Wiener-Neustadt, Austria
Modifications	2 underwing pods for instrumentation (wide enough for 19"/6HU instruments), enhanced MTOW, larger fuel tanks, door to baggage/instrument compartment behind the cockpit, second electrical system with 28V/1 kW generator
Operation	Daytime VFR (avionics accordingly, with Transponder Type S since 2008)
Cruising speed	(minimum / typical / maximum during measurements): 110 / 170 / 200 km/h (IAS)
Climb rate	3 m/s from GND to about 3000 mMSL Typical operation altitudes 150 mGND to 3000 mMSL, or less with special permission
Electrical power	primary 28 VDC unregulated (+/- 1 V) 1 kW (operationally tested up to 0.5 kW); 100 Watt 12 VDC regulated; 300 Watt 230 VAC, power system of the scientific instruments is separated from the aircraft system
Scientific instruments	Laser altimeter (100 Hz, 0.2 m precision, 1 m accuracy) Vertical camera Wind measurement (five-hole probe, accelerometers and a high-grade IMU) Fast thermometer (10 Hz) Dew point mirror Two modified LiCor's Two IR-absorption instruments (modified LI-6262 and LI-7500) a) LI-6262: Reference gas (380 ppm) and N ₂ -flushing (no scrubbers) has a very high accuracy (0.4 ppm), but is slow (about 0.1 Hz), b) LI-7500: fast, but not very accurate (can drift easily by several ppm due to varying aerosols, volume with homogeneous density, measured by pressure- and temperature-sensors in this volume)



Figure 8: Standard flight pattern for Grosseto, Italy. This pattern was repeated up to five times (back and forth) per day (about half an hour per completed run).

Table 11: Flight lines flown by MetAir over Grosseto, Italy during the campaign 2018.

Flights Siena / Grosseto

date	from [LT]	to [LT]	duration	ferry		meas.		Remarks	
				h	min.	h	min.		
18.06.2018	14:47	15:22	00:35	0	35			no laser altimeter (vegetation structure)	
18.06.2018	16:15	19:06	02:51	2	51			no laser altimeter (vegetation structure)	
19.06.2018	11:12	14:56	03:44			3	44		
20.06.2018	10:18	13:57	03:39			3	39		
21.06.2018	10:23	14:20	03:57			3	57	no fast temperature	
22.06.2018	10:22	13:23	03:01	3	1				
22.06.2018	14:01	14:36	00:35	0	35				
02.07.2018	10:04	10:37	00:33	0	33				
02.07.2018	11:08	14:03	02:55	2	55				
03.07.2018	10:39	14:30	03:51			3	51		
04.07.2018	10:20	13:43	03:23			3	23		
04.07.2018	16:20	19:14	02:54	2	54				
04.07.2018	19:34	20:11	00:37	0	37				
18.07.2018	09:59	10:35	00:36	0	36				
18.07.2018	11:04	15:23	04:19	3	19	1	0		
19.07.2018	10:53	14:43	03:50			3	50	including CH ₄	
20.07.2018	10:53	15:07	04:14			4	14	including CH ₄	
21.07.2018	14:11	16:23	02:12			2	12	including CH ₄ and FloxBox	
22.07.2018	11:18	13:34	02:16			2	16	including CH ₄ and FloxBox	
23.07.2018	12:53	14:48	01:55			1	55	including CH ₄ and FloxBox	
24.07.2018	10:21	13:28	03:07			3	7	including CH ₄ and FloxBox	
24.07.2018	16:10	19:00	02:50	2	50				
24.07.2018	19:22	19:56	00:34	0	34				
flight hours for ferry and for measurements				21.33		37.13		12 measuring days	

	Doc.: Photosynthesis report Version1		
	Date: 27.11.2019	Issue: 2	Revision: 1
	Ref.: ESA Contract No. ESA RFP/3-15506/18/NL/NF		Page: 26 / 69

2.3.4 Ground-based high-performance point spectrometers for continuous measurements – FloX system

The D-FloX represents the evolution of the systems reported in Cogliati et al. (2015) and in Burkart et al. (2015) which have been used in the past as ground validation of *HyPlant* sensor. The D-FloX is designed for high temporal frequency acquisition of continuous top of canopy (TOC) radiometric measurements. The system is equipped with two spectrometers: i) Ocean Optics FLAME S, covering the full range of visible and near-infrared (VIS-NIR); ii) Ocean Optics QEPro, with high spectral resolution (Full Width at Half Maximum – FWHM - of 0.3 nm) in the range of the fluorescence emission 650 nm – 800 nm. Each spectrometer's optical input is split towards two fibre optics, that lead to 1) a cosine receptor measuring the sun irradiance and 2) a bare fibre measuring the target reflected radiance. Spectrometers are housed in a Peltier thermally regulated box keeping the internal temperature lower than 25 °C in order to reduce dark current drift. Moreover, the Thermoelectric cooler (TEC) of QEPro is set to 20 °C in order to always provide stable measurements. The signal is automatically optimized for each channel at the beginning of each measurement cycle and two associated dark spectra are collected as well. Metadata such as spectrometer temperature, detector temperature and humidity are also stored in the SD memory of the system. The measurements are fully automatically. After setup and activation, no further user input is required. D-FloX is optimized for low power consumption and remote installation with multiple interfaces for data storage and transmission.

Several FloX are installed permanently on various sites (see also AtmoFLEX campaign for details of the FloX systems in Germany and Italy). Additionally, there is a mobile FloX at the German site. This FloX can be carried within the fields and between different plots, allowing mobile measurements of many fields during the time of overpass (see FlexSense campaign for details).

2.3.4.1 FloX located in Selhausen, Germany

At the Selhausen site (EC-Tower (EC-04) on the winter wheat field near Selhausen), a previous version to the FloX system was installed. This so-called SIF-Sys-Box was installed over the entire growth period 2018. The SIF-Sys Box differs from a FloX by having only one spectrometer, which covers the full range from 400 - 900 nm with a spectral sampling interval of 0.78 nm and spectral resolution (FWHM) of ~ 1 nm. On May 15th, an additional FloX (JB-011-JF) was installed at the same location with the same FOV, so that from this date the values of both devices are available. Since FloX data is only available after June 15th, 2018, the data from the SIFSys Box-4 may be used to cover the entire growth period.

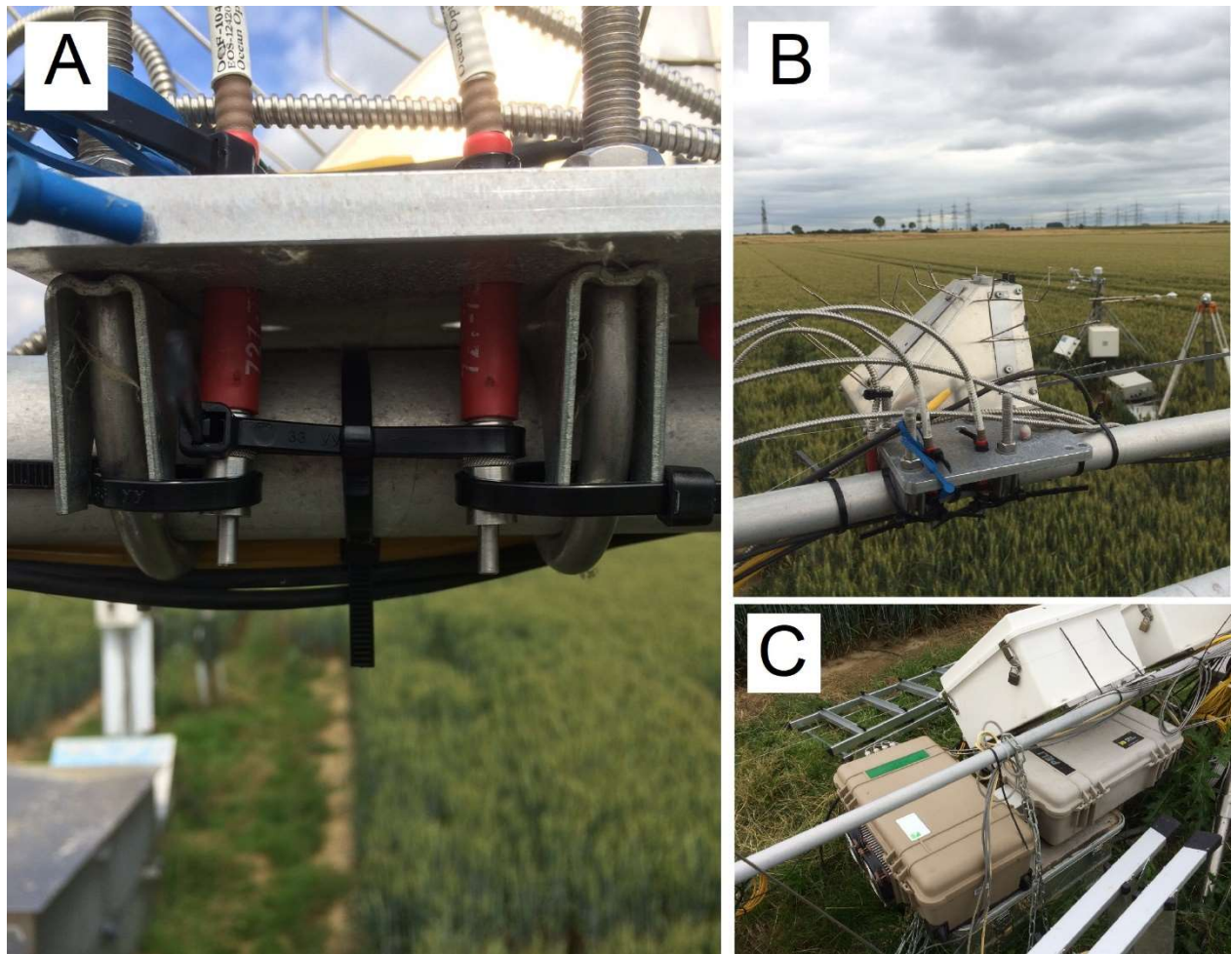


Figure 9: Position of FloX JB-011-JF and SIFSys Box-4 next to the EC-Tower (EC04) in a winter wheat field next to Selhausen, Germany. A) Fibres pointing downwards directly next to each other; B) Overview of the fibre positioning. The cosine receptors for the measurement of incident radiation can be seen. C) The two boxes are positioned directly next to each other.

The iFLD method has been used in both cases (data from FloX JB-011-JF and SifSys Box-4) to retrieve the fluorescence products. However, it has already been noted that due to the low spectral resolution of the SIFSys Box-4 the derivation of the fluorescence product F687 may be difficult. Thus, a detailed intercomparison between the two systems was performed.

Comparison of data from FloX and SIFSys box¹

PAR values of the two boxes (blue: FloX JB-011-JF and orange: SIFSys Box-4) were processed of a day with changing light (14th of June, Figure 15) and clear sky conditions (29th of June, Figure 16).

¹ This sub-chapter may be moved into the supplementary material in later versions of the Photosynthesis report, but is reported in detail here as it is a valuable intermittent step that will enable us to extend the time series that are available for this study.

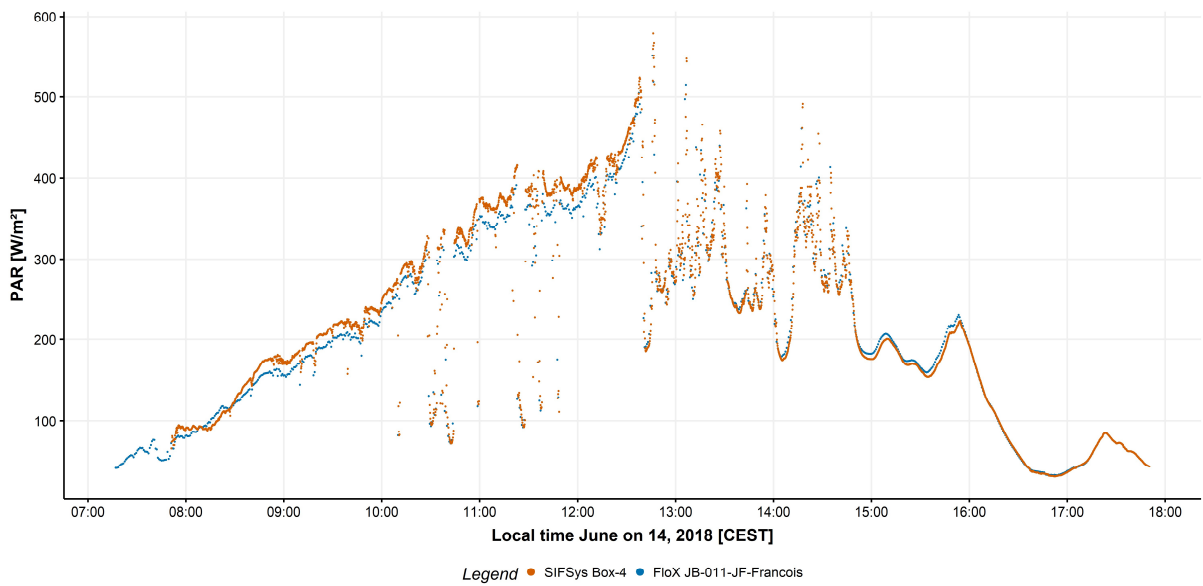


Figure 10: PAR values from June 14th, 2018 processed from the FloX JB-011-JF (blue) and the SIFSys Box-4 (orange).

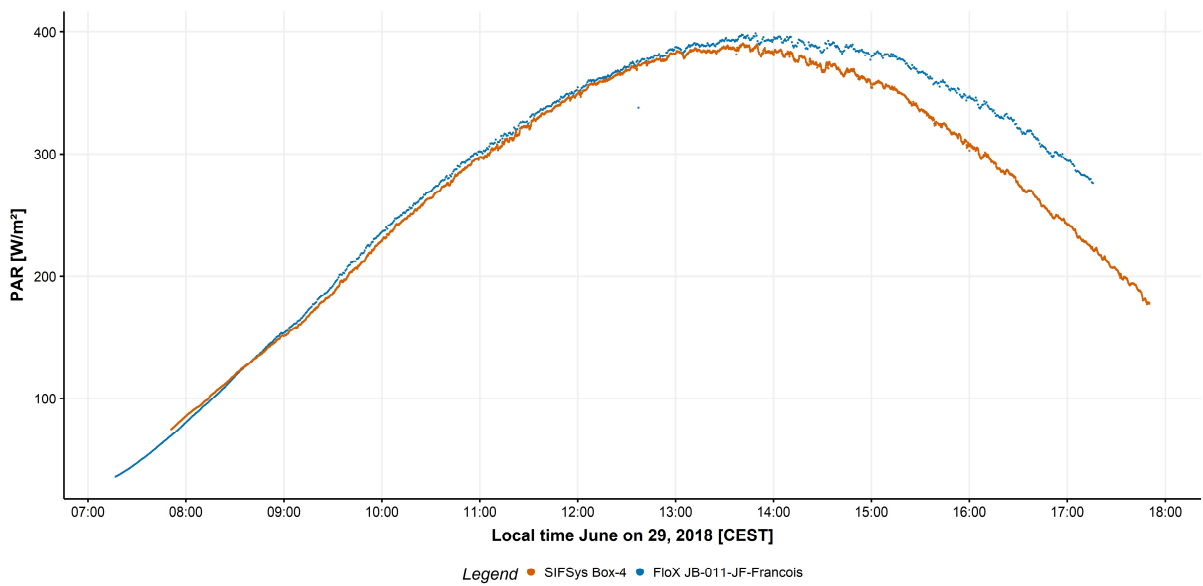


Figure 11: PAR values from June 29th, 2018 processed from the FloX JB-011-JF (blue) and the SIFSys Box-4 (orange).

While the PAR values of both devices hardly differ under changing light conditions (Figure 10, 14th of June), under stable light conditions (Figure 11, 29th of June) an offset after 1 PM is apparent.

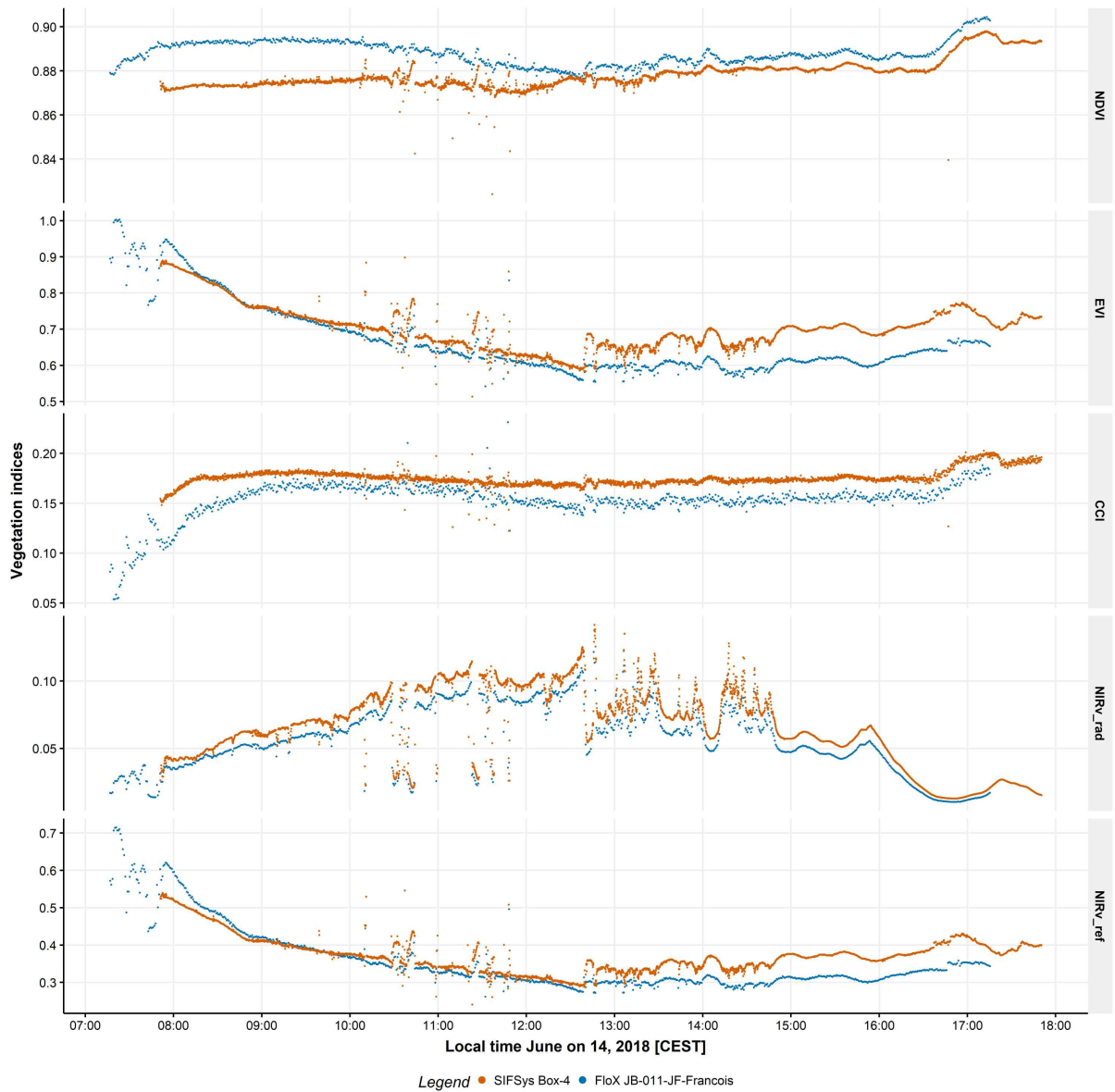


Figure 12: Vegetation indices (Top to bottom: NDVI, EVI, CCI, NIR_{rad} (NDVI*L₈₀₀), NIR_{v_ref} (NDVI*R₈₀₀) from June 14th, 2018 processed from the FloX JB-011-JF (blue) and the SIFSys Box-4 (orange).

The two devices output slightly different absolute values for 14th of June. At which times of the day the curves lie on top of each other and when they deviate varies according to VI. In comparison, the FloX outputs have up to 0.02 higher values for the NDVI during the day, while it outputs lower values for the other indices. The EVI is up to 0.1 lower in the afternoon, the CCI about 0.03 lower during the day, the NIR_{rad} about 0.01 lower during the day and the NIR_{v_ref} about 0.08 lower in the afternoon. These differences are hardly relevant in relation to the total value range of the indices. The trend in the course of the day is mapped very similarly by both devices (Figure 12).

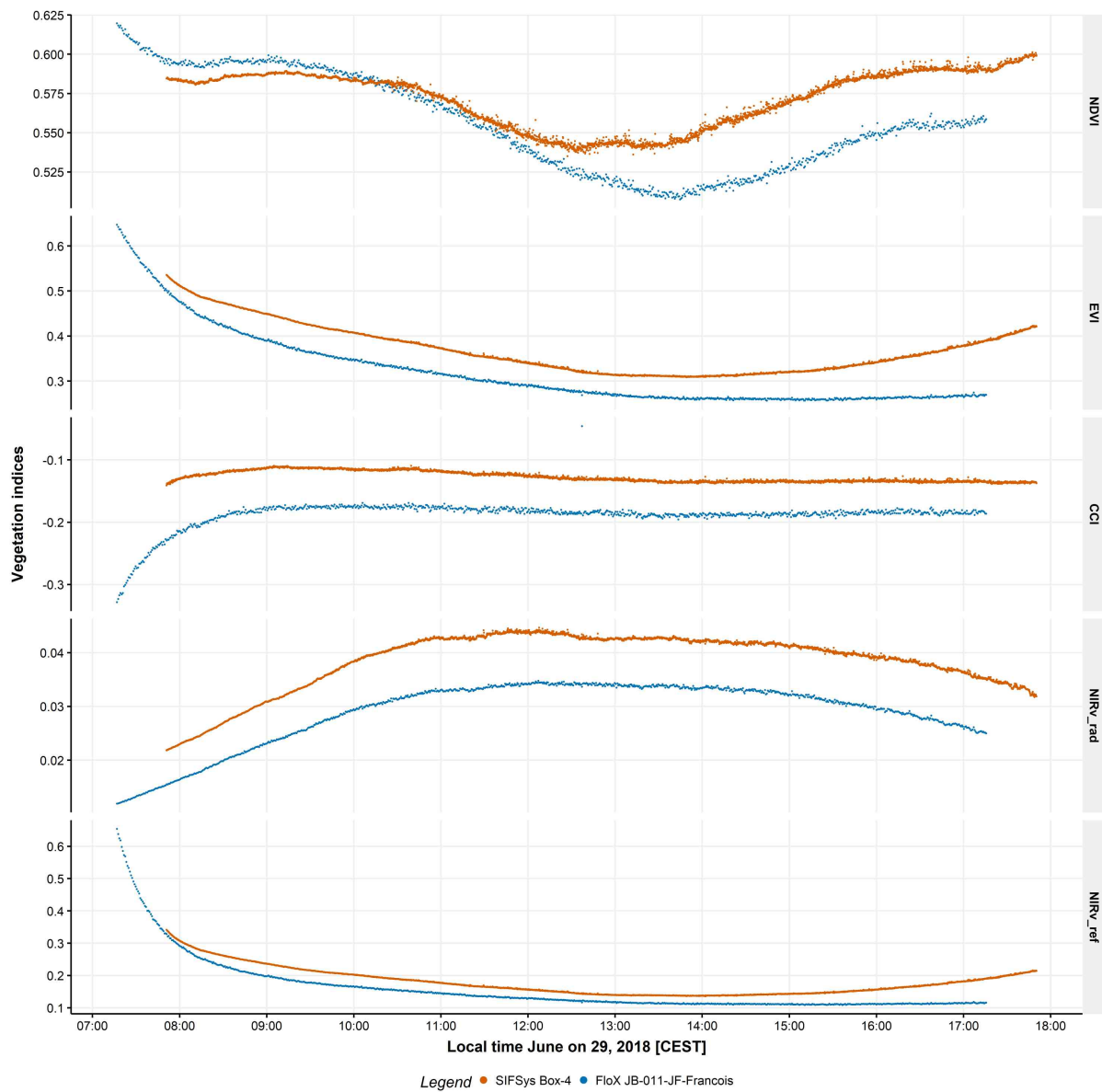


Figure 13: Vegetation indices (Top to bottom: NDVI, EVI, CCI, NIR_{rad} (NDVI * L₈₀₀), NIR_{v_ref} (NDVI * R₈₀₀) from June 29th, 2018 processed from the FloX JB-011-JF (blue) and the SIFSys Box-4 (orange).

Under cloudless conditions on June 29th, the differences of the processed VI's tend to be the same as under changing light conditions and the absolute value differences are even smaller (Figure 13).

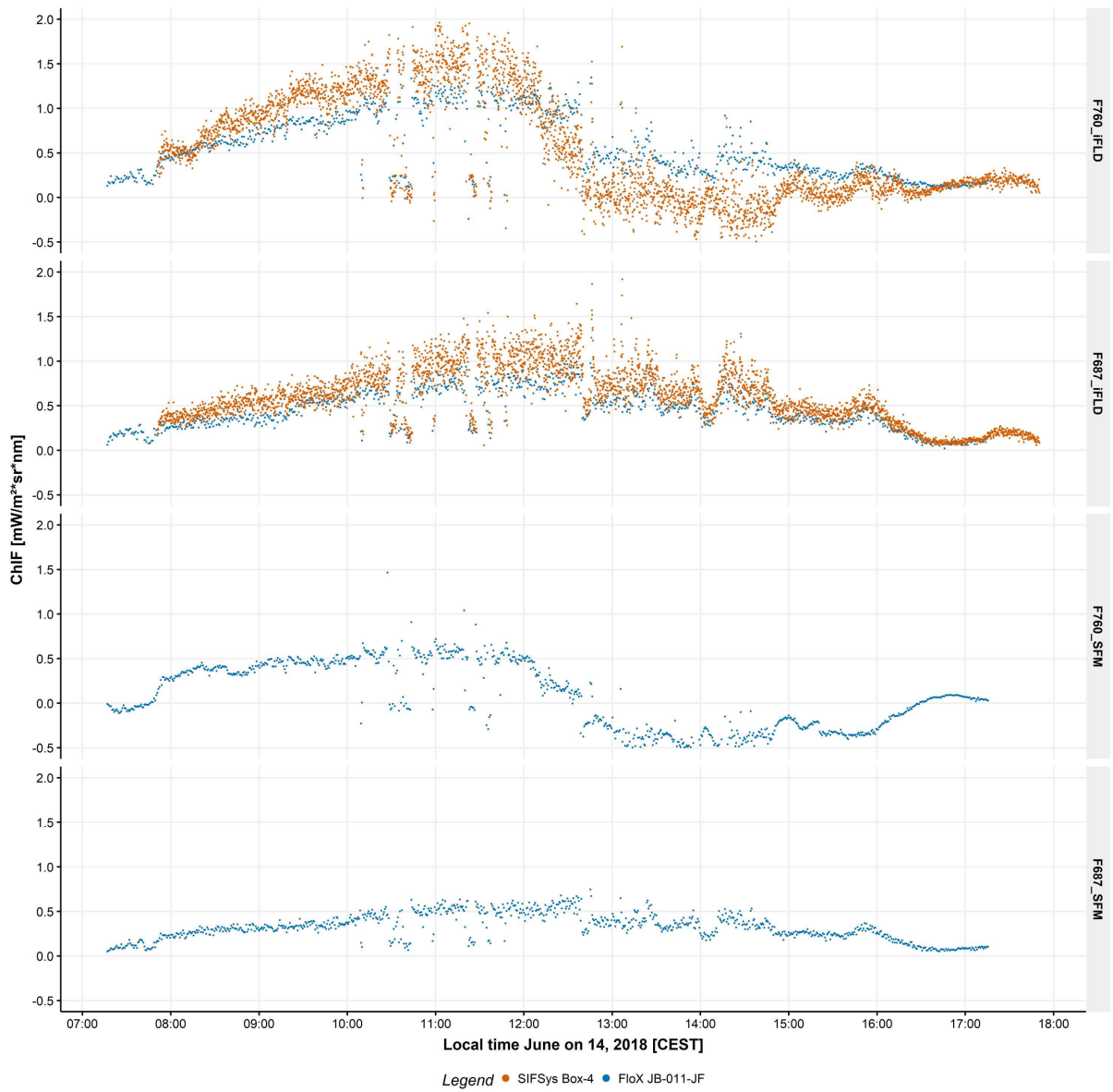


Figure 14: F760 and F687 (Top to bottom: retrieved from iFLD, retrieved from SFM) from June 14th, 2018 processed from the FloX JB-011-JF (blue) and the SIFSys Box-4 (orange).

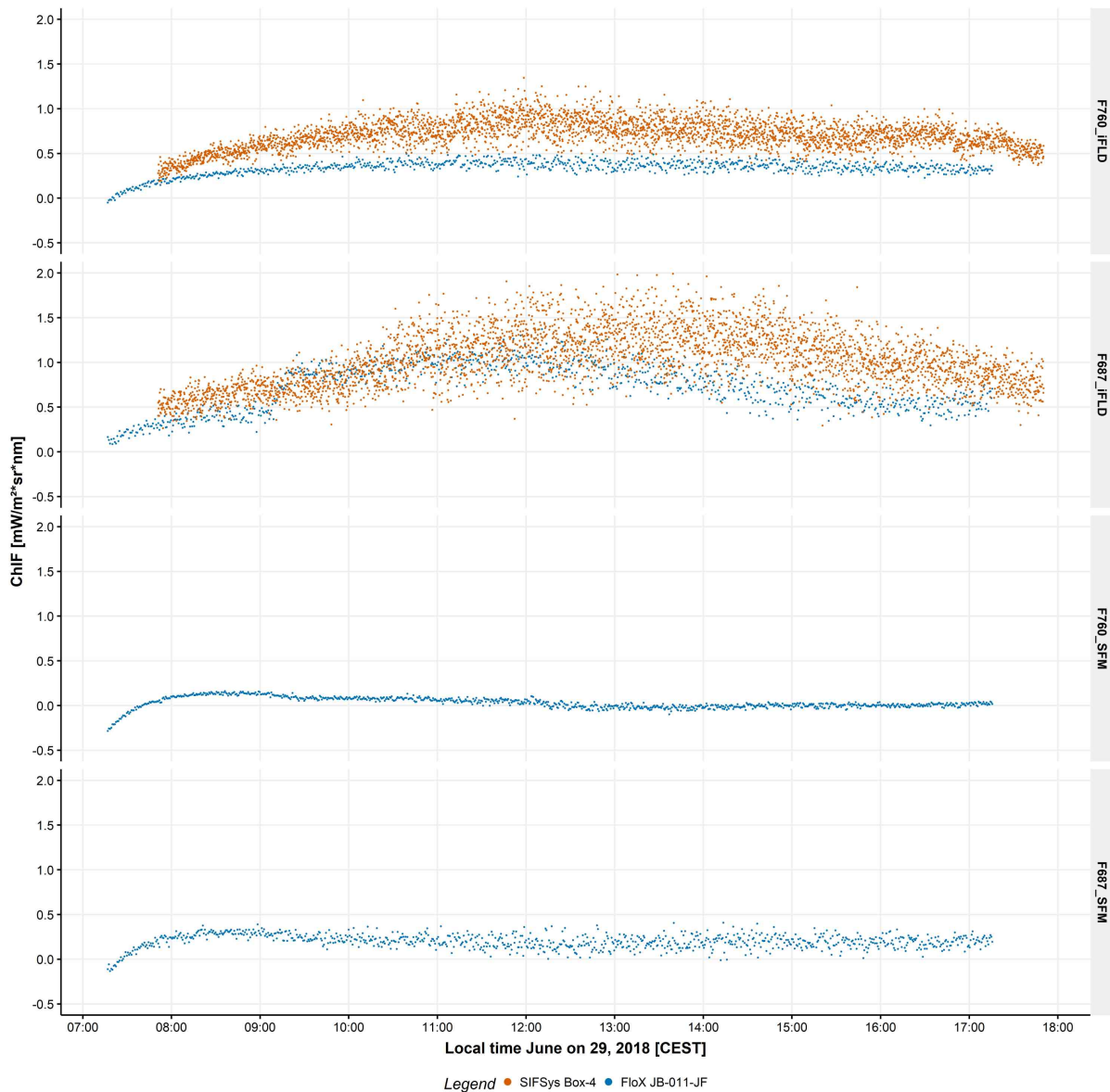


Figure 15: F760 and F687 (Top to bottom: retrieved from iFLD, retrieved from SFM) from June 29th, 2018 processed from the FloX JB-011-JF (blue) and the SIFSys Box-4 (orange).

In Figure 14 and 15 it becomes apparent that no values are available for the SFM retrieval of F_{760} and F_{687} for SIFSys Box-4. This is due to the too low spectral resolution of this device, which makes the application of this retrieval method unsuitable (see Material and Methods). Furthermore, the noise is higher with both SIF products (retrieved from iFLD method). However, the temporal resolution is also higher, since this box has a faster integration time due to the lower spectral resolution. In order to describe seasonal trends with the SIFSys SIF products, the F_{760} and F_{687} can be averaged to remove the noise. It is advisable to use data from the FloX to evaluate the daily trends.

The comparison of the two devices (FloX JB-011-JF and SIFSys located next to Selhausen, Germany) has shown that basically, the data of the spectrally lower resolved SIFSys can be used to evaluate the times at which no FloX data is available. However, the application of a filter to the FloX and SIFSys data is necessary to exclude unreliable data. These include, for example, values at which shadow effects by the canopy cannot be excluded, or artefacts of the "cosine receptor". This applies to measurements at lower sun elevations, i.e. in the early morning hours and late afternoon. As a next step, a filter scheme will be developed. In order to investigate seasonal trends in the data from Selhausen, Germany,

	Doc.: Photosynthesis report Version1		
	Date: 27.11.2019	Issue: 2	Revision: 1
	Ref.: ESA Contract No. ESA RFP/3-15506/18/NL/NF		Page: 33 / 69

fluorescence products will need to be averaged from the SIFSys data. The next step is to determine whether the preferred method is, for example, the average over the course of the day, an integral over the course of the day, or to choose values of solar noon.

2.3.4.2 *FloX located in Lincoln, United States*

The University of Nebraska operates a D-FloX system similar to that deployed in Selhausen. The instrument is mounted on a scaffolding tower located in an agricultural field (NE-3) in the footprint of the eddy covariance tower (Figure 4). Specifications are similar to that of the Selhausen D-FloX except for the following differences:

- The original fibers have been replaced by low OH 600um, 0.39 NA fibers from Thorlabs (FT600EMT).
- The upwelling fibers were stopped down to a 25 degrees field of view using a black polycarbonate 3D printed holder.
- The downwelling fibres were equipped with a thick Teflon cosine corrector (CR2, Stellarnet).
- The radiance calibration of the whole system was performed in an integrating sphere at eight different levels of light.

2.3.4.3 *FloX located in Majadas, Spain*

The FloX in Majadas, Spain were designed and built by JB Hyperspectral Devices. Overall, they have the same specifications and output as the FloX used in Selhausen.

2.3.4.4 *FloX located in Grosseto, Italy*

The FloX in Grosseto, Italy were designed and built by JB Hyperspectral Devices. Overall, they have the same specifications and output as the FloX used in Selhausen.

2.3.5 Ground based eddy covariance and ancillary measurements

In the framework of the Integrated Carbon Observation System (ICOS), three EC towers are positioned in three different locations in Germany. This is the German contribution for the European network infrastructure of the monitoring system ICOS. In Germany, the EC towers are meant for atmospheric measurements of CO₂, CH₄ and N₂O. Since 2015, the IBG-3 operates an EC tower on the Selhausen field site. The EC tower was equipped with a three-dimensional sonic anemometer (Model CSAT-3, Campbell Scientific Inc., Logan, Utah, USA) and an open path infrared gas analyser (Model LI-7500, Li-Cor Inc. Biosciences, Lincoln, Nebraska, USA). The analyser was calibrated every three months in the lab. Both instruments were mounted 2.5 m above the surface. EC measured turbulent fluxes were calculated as 30-min averages using the software package TK3.11 (Mauder and Foken 2011). The test field was additionally equipped with meteorological measurements like air temperature (HMP45C, Vaisala Inc., Helsinki, Finland) precipitation (Thies Clima type tipping bucket, distributed by Ecotech, Bonn, Germany) and radiation (NR01, Hukseflux, Delft, Netherlands). Up to four self-calibrating soil heat-flux plates (HFPO1, Hukseflux Thermal Sensors, Delft, Netherlands) were installed at a depth of 0.08 m. Soil water content (SWC, CS616, Campbell Scientific, Inc., Logan, USA) and soil temperature (TCAV, Campbell Scientific, Inc., Logan, USA) were sampled in the layer above the heat flux plates. All measurements were performed in the immediate vicinity of the EC station. Beside the flux

	Doc.: Photosynthesis report Version1		
	Date: 27.11.2019	Issue: 2	Revision: 1
	Ref.: ESA Contract No. ESA RFP/3-15506/18/NL/NF		Page: 34 / 69

measurements and typical climate parameters, also the phenological development of the crops and farming activities were recorded. The here used EC tower is from a field where winter wheat was growing during the vegetation period 2018. The climate is mainly moderate with a mean value for the year's temperature of 10 °C. The average of the year's precipitation lies around 700 mm.

2.3.6 Ground based vegetation measurements

Samples were taken at Selhausen, Germany. The cultures sampled were barley, sugar beet, maize, potato, wheat, and pea. Sampling was done in July and August, 2018. The data acquired in the field were the developmental stage using the BBCH scale, plant height, sowing density and Chlorophyll content using a SPAD-502Plus Chlorophyll meter (Konika Minolta Inc., Japan). For the SPAD measurements, the average of ten leaf measurements was determined. Additionally, whole plant samples were taken and stored in a plastic bag in order to determine the fresh weight on the same day at the Jülich Research Centre. The leaf area was measured using a Li-3200C Area Meter (LI-COR, USA). The samples were then stored at 65° C until they were dry in order to determine dry weight.

For the determination of the Chlorophyll and Carotenoid content, fresh green leaves were sampled in the field. Using a leaf tissue puncher, 3 - 5 leaf disks with a diameter of 8 mm were randomly punched out of the upper green leaves of a plant. The leaf disks were transferred into 2-ml microcentrifuge tubes, immediately frozen in liquid nitrogen and transported to the Jülich Research Centre. The samples were then stored at -80° C.

The leaf disk samples acquired in the field and stored at -80° C were weighed into 2-ml microcentrifuge tubes with a weight between 10 mg and 20 mg. The extraction of chlorophyll A, chlorophyll B and carotenoids was performed with 100 % Acetone buffered with Magnesium hydroxide carbonate (~4MgCO₃ · Mg(OH)₂ · 5 H₂O). 10 g of Magnesium hydroxide carbonate were mixed with 500 ml of Acetone and stored at 4° C. 250 µl of the described buffer were added to the previously weighed leaf disk including a metal sphere. Homogenization was done using the swing mill MM 400 (Retsch, Germany) for 60 s at a frequency of 30 s⁻¹. The metal ball was removed using a magnet and washed three times with 250 µl Acetone buffer that was captured in the microcentrifuge tube. The tubes were then centrifuged at 4° C at 4100 rpm for 5 min.

250 µl of the supernatant were transferred into a Cuvette and mixed with 750 µl Acetone 100 % (dilution 1:4). Absorption was measured with a Specord 200 Plus spectrophotometer (Analytik Jena AG, Germany). The measurements were performed at the wavelengths 470 nm, 645 nm, 662 nm, and 710 nm. During all steps, starting at the extraction, the tubes were exposed to as little light as possible and continuously stored on ice until measurement.

For the determination of the Chlorophyll and Carotenoid content, the absorbance values in the following equations as described in Lichtenthaler and Buschmann (2001) and Lichtenthaler (1987) were substituted with the acquired values:

$$\text{Chl}_A = 11.24 (A_{662} - A_{710}) - 2.04 (A_{645} - A_{710})$$

$$\text{Chl}_B = 20.13 (A_{645} - A_{710}) - 4.19 (A_{662} - A_{710})$$

$$\text{Chl}_{A+B} = 7.05 (A_{662} - A_{710}) - 18.09 (A_{645} - A_{710})$$

$$\text{Bulk Carotenoids} = (1000 (A_{470} - A_{710}) - 1.9 \text{Chl}_A - 63.14 \text{Chl}_B) / 214$$

	Doc.: Photosynthesis report Version1		
	Date: 27.11.2019	Issue: 2	Revision: 1
	Ref.: ESA Contract No. ESA RFP/3-15506/18/NL/NF		Page: 35 / 69

2.4 Data processing

2.4.1 Calculation of vegetation products

The different remote sensing products, vegetation Indices and sun-induced fluorescence, examined in this study have been developed in most cases for a certain spatial resolutions e.g. space, airborne, top-of-canopy.

While the application of NDVI and EVI have had experiences with satellite, airborne and ground-based systems over the past decades, CCI has so far only been recently available from MODIS, although it can readily be calculated from hyperspectral sensors from other platforms (Gamon et al., 2016). The same applies to the NIRv (Joiner et al., 2018).

2.4.1.1 Description of the used vegetation indices

Normalized difference vegetation index (NDVI)

NDVI is perhaps the best known and most commonly used vegetation index to quantify green vegetation. It reliably differentiates between vegetation and soil and minimizes topographic influences (Huete et al., 2002; Sotomayor, 2002). It correlates well with canopy features such as biomass, leaf area index (LAI), APAR and canopy photosynthetic capacity (Gamon et al., 1992 and Sellers et al., 1987).

The index relies on two wavebands only as can be seen in equation (1).

$$NDVI = \frac{NIR - RED}{NIR + RED} \quad (1)$$

Where RED = 620 to 700 nm (around 670) and NIR = approx. 800 nm

NDVI is unitless and ranges from -1 to 1. Negative values are associated with water bodies. NDVI assumes relatively high values (0.3 - 0.6) over well overgrown targets and saturates over dense green canopies such as rain forests or intensively managed agricultural crops (Verstraete and Pinty, 1996).

The following equation (2) shows a common formulation of NDVI that is proposed to be used as far as possible in all instruments and platforms.

$$NDVI = \frac{R_{795-810} - R_{665-6}}{R_{795-810} + R_{665-6}} \quad (2)$$

R_x denotes the reflectance at this specific wavelength.

Enhanced vegetation index (EVI)

The EVI was further development based on NDVI to be used in areas where the LAI is high and NDVI saturates. It was developed on MODIS bands and is taking into consideration an additionally blue waveband as can be seen in equation (3) (Verstraete and Pinty, 1996).

$$EVI = G * \frac{NIR - RED}{NIR + C_1 * RED - C_2 * BLUE + L} \quad (3)$$

Where p is atmospherically corrected or partially atmospherically corrected surface reflectance, L is the canopy background adjustment that addresses nonlinear, differential NIR and red radiant transfer through a canopy, and C1, C2 are the coefficients of the aerosol resistance term, which uses the blue band to correct for aerosol influences in the red band.

	Doc.: Photosynthesis report Version1		
	Date: 27.11.2019	Issue: 2	Revision: 1
	Ref.: ESA Contract No. ESA RFP/3-15506/18/NL/NF		Page: 36 / 69

EVI is unitless and ranges from -1 to 1 and healthy vegetation generally falls between values of 0.2 – 0.8. While NDVI saturates in high-biomass regions, such as tropical rainforests, EVI remains sensitive to canopy variations (Huete et al., 2002).

The following equation (4) shows a common formulation of EVI that is proposed to be used as far as possible in all instruments and platforms.

$$EVI = 2.5 \frac{R_{795-810} - R_{665-680}}{R_{795-810} + 6 * R_{665-680} - 7.5 * R_{475-490} + 1} \quad (4)$$

Chlorophyll/Carotenoid Index (CCI)

CCI was proposed by Gamon et al., 2016 as an indicator of seasonally changing chlorophyll and carotenoid pigment rations. CCI is essentially a modification of the Photochemical Reflectance Index (PRI), which tracks diurnal changes in xanthophyll cycle pigment activity. PRI uses reflectance at 531 nm and a different reference wavelength at 570 nm (see eq. 5) and is designed to track short-term reflectance changes at 531 nm due to the xanthophyll cycle, and indicator of photosynthetic light efficiency (Gamon et al, 1992). The reference wavelength is used to minimize complications associated with diurnal sun angle changes (Gamon et al, 1992).

$$PRI = \frac{R_{REF} - R_{531}}{R_{REF} + R_{531}} \quad (5)$$

As the original PRI bands are not available from MODIS, Gamon et al., 2016 considered new MODIS band combinations (bands 1 and 11) indicative of chlorophyll / carotenoid ratios and developed the CCI, sometimes called as “MODIS PRI”. As for the PRI, for the calculation of the CCI the reflectance around 531 nm is used which is proximal to the absorption band of xanthophyll pigment.

$$CCI_{MODIS} = \frac{\rho_{B11} - \rho_{B1}}{\rho_{B11} + \rho_{B1}} \quad (6)$$

CCI is unitless and ranges from -1 to 1.

These new band combinations are spectrally and functionally different from original PRI bands. While PRI was designed to track short-term reflectance at 531 nm, CCI is primarily responding to changing pigment pools, which can be indicative of seasonally changing photosynthetic rates (Gamon et al, 2016). This relationship has primarily been tested in evergreen conifers (where NDVI or EVI cannot provide a reliable indicator of seasonal photosynthetic activity), and further tests in other vegetation types are warranted.

Near-infrared reflectance of vegetation (NIRv)

NIRv is a product of total scene NIR reflectance (NIR_T) and the NDVI and represents the proportion of pixel reflectance attributable to the vegetation in the pixel, which better normalizes for variations in background reflectance than NDVI or (NIR_T alone (Badgley et al, 2017).

$$NDVI = NDVI * NIR_T \quad (7)$$

NIRv ranges from 0 – Inf and is unitless.

In Badgley et al, 2017, NIRv was calculated using reflectance for NIR_T as this available from satellite data.

	Doc.: Photosynthesis report Version1		
	Date: 27.11.2019	Issue: 2	Revision: 1
	Ref.: ESA Contract No. ESA RFP/3-15506/18/NL/NF		Page: 37 / 69

$$\text{NIRv}_{\text{MODIS}} = \left(\frac{\rho_{B2} - \rho_{B1}}{\rho_{B2} + \rho_{B1}} - C \right) * \rho_{B2} \quad (8)$$

In Badgley et al, 2017 NIRv ranges from 0 to 0.5 and is unit less.

However, it is argued that whenever radiance is available, it should be used, as it is likely to be the true basis for the correlations they describe. Therefore, if the data allows, a hybrid calculation with near-infrared reflectance and radiance is preferred. In case NIRv is calculated based on radiance measurements, a correction factor is needed to account for differences in the downwelling radiance in the red and NIR bands.

2.4.1.2 Calculation of Vegetation Indices from FloX

Vegetation indices are calculated from FloX data based on the bandmath function. The VIs band are calculated around the center band + or - FWHM/2. According to the convolution specified the mean or a Gaussian convolution is calculated and used to compute the VI. Generally, mean convolution is used here. Exceptions are mentioned.

Filtering schemes for vegetation indices and SIF are mainly based on stability of the irradiance and the SZA. E_stability (parameter informing about the change in irradiance during a cycle of measurement) >0 and E_stability <= 0.25 and SZA < 50. Additional filtering criteria are based on whether the spectrometer saturated during the measurements or on the convergence of the spectra fitting method (SFM) retrieval technique.

Calculation of NDVI

$$\text{NDVI}_{\text{FloX}} = \frac{R_{<795-805>} - R_{<665-675>}}{R_{<795-805>} + R_{<665-675>}} \quad (9)$$

R_x denotes the reflectance at this specific wavelength.

Calculation of EVI

$$\text{EVI}_{\text{FloX}} = 2.5 \left[\frac{R_{<795-805>} - R_{<665-675>}}{R_{<795-805>} + 6 \cdot R_{<665-675>} - 7.5 \cdot R_{<475-485>} + 1} \right] \quad (10)$$

R_x denotes the reflectance at this specific wavelength.

Calculation of CCI

There is no established protocol yet to derive CCI from FloX. The calculation of the CCI is based on MODIS band 1 (wavelength: 620-670 nm) and band 11 (wavelength 526-536 nm) (see eq. 25, Band 11) was chosen to depict the reflectance at 531 nm according to PRI. If possible, a narrow wavelength range should be used (Gamon et al 1992, Gamon et al 2016). Whereas band 1 in the range from 620 to 670 nm represents the changes of the pigment pool and covers a wider wavelength range.

$$\text{CCI}_{\text{MODIS}} = \frac{\rho_{B11} - \rho_{B1}}{\rho_{B11} + \rho_{B1}} \quad (25)$$

Since FloX have a higher spectral resolution than the MODIS satellite, a smaller spectral range can be selected, especially as a replacement for Band 11. Therefore, the central wavelengths to be used for CCI were defined as

$$CCI_{FloX}^* = \frac{\rho_{531} - \rho_{645}}{\rho_{531} + \rho_{645}} \quad (26)$$

Five different spectral ranges (2, 4, 6, 8, and 10 nm) for the wavelength around 645 nm were tested to see possible differences in the use of narrow or wider wavelength ranges in the calculation of the equivalent of MODIS Band 1.

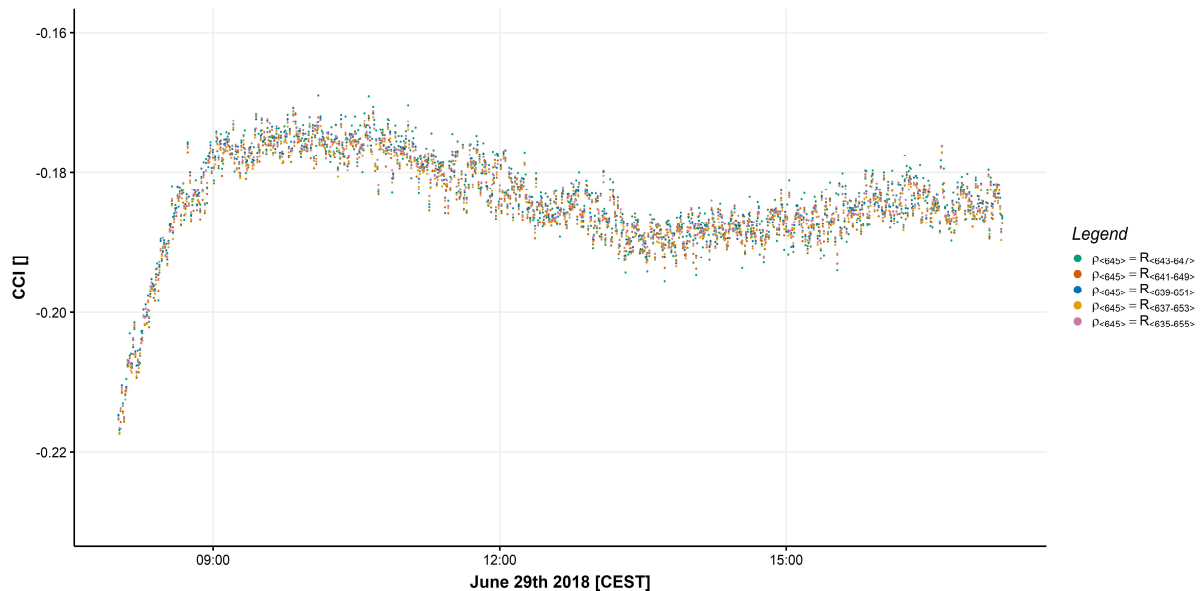


Figure 16: Calculation of different CCI's based on 5 different spectral ranges for ρ_{645} . ρ_{645} was calculated with 2,4,6,8 and 10 nm spectral range. Shown is the daily course from June 29th, 2019 (clear sky conditions). The data were measured with FloX JB-011-JF next to the ICOS tower in Selhausen, Germany.

The results were hardly different and therefore a spectral range of 10 nm around 645 nm is proposed to be used for calculating CCI from FloX leading to the following formula:

$$CCI_{FloX} = \frac{R_{<531>} - R_{<635-655>}}{R_{<531>} + R_{<635-655>}} \quad (27)$$

R_x denotes the reflectance at this specific wavelength.

Calculation of NIRv

So far, there is no established protocol yet to derive NIRv from FloX. NIRv, based on same wavelengths as NDVI, was developed based on MODIS.

To calculate the NIRv based on radiance (NIRv_rad) a two-stage calculation is necessary. Reflectance-based NDVI is implemented in the standard processing pipeline and subsequently multiplied by the radiance at 800 nm " L_{800} ".

$$NIRv_{rad}_{FloX} = \frac{R_{<795-805>} - R_{<665-675>}}{R_{<795-805>} + R_{<665-675>}} * L_{800} \quad (29)$$

Five different spectral ranges from small (2 nm) to broad (10 nm) were calculated for L_{800} on the record of FloX JB-011-JF from 14th – 30th June 2018 to test the influence of the width of the spectral range.

Based on the results of this comparison (see results section), we propose the following formula to calculate the NIRv_rad of FloX data.

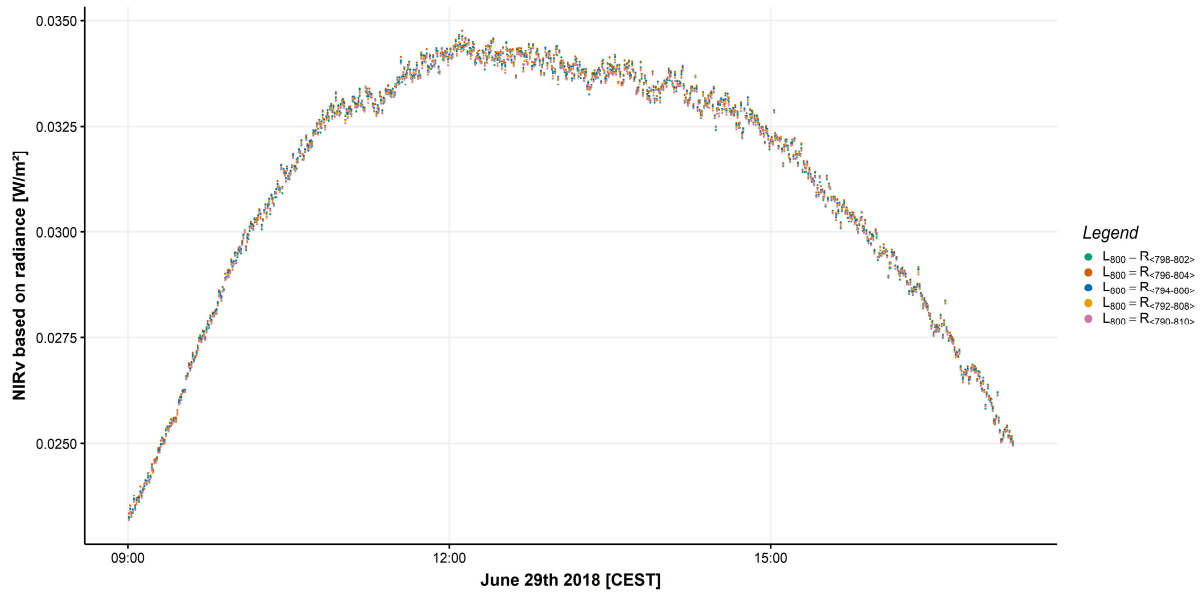


Figure 17: Calculation of different NIRv_rad's based on 5 different spectral ranges for L₈₀₀. L₈₀₀ was calculated with 2,4,6,8 and 10 nm spectral range. Shown is the daily course from June 29th, 2019 (clear sky conditions). The data were measured with FloX JB-011-JF next to the ICOS tower in Selhausen, Germany.

The results were hardly different and therefore a spectral range of 10 nm for L₈₀₀ is proposed to be used for calculating NIRv_rad from FloX leading to the following formula:

$$NIRv_{rad_{FloX}} = \frac{R_{<795-805>} - R_{<665-675>}}{R_{<795-805>} + R_{<665-675>}} * L_{<795-805>} \quad (30)$$

R_x denotes the reflectance at this specific wavelength. L_x denotes the Top-of-canopy radiance at this specific wavelength.

Another calculation of NIRv based on reflectance around 800 nm (NIRv_ref) was done using reflectance values for NIR_T and again testing the influence of the width of the spectral range.

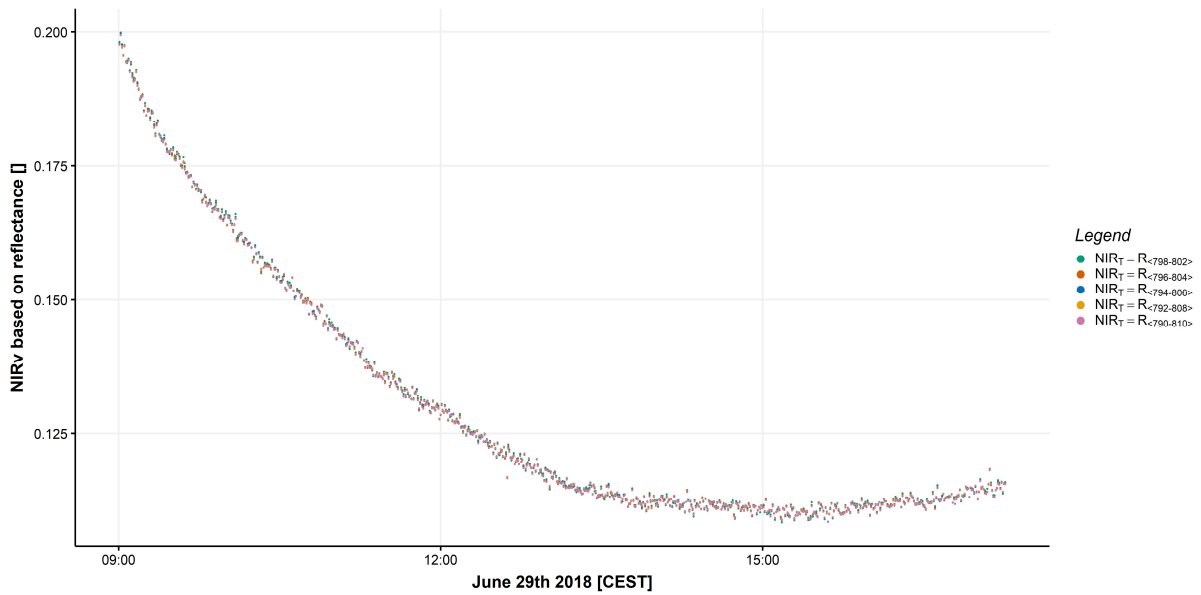


Figure 18: Calculation of different NIRv_ref's based on 5 different spectral ranges for NIR_T. NIR_T was calculated with 2,4,6,8 and 10 nm spectral range. Shown is the daily course from June 29th, 2019 (clear sky conditions). The data were measured with FloX JB-011-JF-Francois next to the ICOS tower in Selhausen, Germany.

The results were hardly different and therefore, a spectral range of 10 nm for NIR_T is proposed to be used for calculating NIRv_ref from FloX leading to the following formula:

$$NIRv_{ref_{FloX}} = \frac{R_{<795-805>} - R_{<665-675>}}{R_{<795-805>} + R_{<665-675>}} * R_{<795-805>} \quad (31)$$

R_x denotes the reflectance at this specific wavelength.

2.4.1.3 Calculation of Vegetation Indices from HyPlant

Calculation of NDVI

$$NDVI_{HyPlant} = \frac{R_{<795-810>} - R_{<665-680>}}{R_{<795-810>} + R_{<665-680>}} \quad (14)$$

R_x denotes the reflectance at this specific wavelength. The spectral windows correspond to 9 bands in HyPlant (central wavelength ± 4 bands).

Calculation of EVI

$$EVI_{HyPlant} = 2.5 \left[\frac{R_{<795-810>} - R_{<665-680>}}{R_{<795-810>} + 6 \cdot R_{<665-680>} - 7.5 \cdot R_{<475-490>} + 1} \right] \quad (15)$$

R_x denotes the reflectance at this specific wavelength. The spectral windows correspond to 9 bands in HyPlant (central wavelength ± 4 bands).

Calculation of CCI

For the calculation of the index from HyPlant, there is no standard protocol/official approach yet. To calculate the CCI of HyPlant data, we propose the following formula:

$$CCI_{HyPlant} = \frac{R_{<531>} - R_{<640-655>}}{R_{<531>} + R_{<640-655>}} \quad (16)$$

R_x denotes the reflectance at this specific wavelength. For $R_{<531>}$, we propose to use a spectral window of 3 bands (center wavelength ± 1 band). The spectral window of $R_{<640-655>}$ corresponds to 9 bands (center wavelength ± 4 band).

Calculation of NIRv

For the calculation of the NIRv from *HyPlant*, there is no standard protocol/official approach yet. To calculate the NIRv of *HyPlant* data, we propose the following formula:

$$NIRv_{HyPlant} = \frac{R_{<795-810>} - R_{<665-680>}}{R_{<795-810>} + R_{<665-680>}} * L_{<800>} \quad (17)$$

R_x denotes the reflectance at this specific wavelength. The spectral windows correspond to 9 bands in *HyPlant* (central wavelength ± 4 bands). L_x denotes the TOC radiance at this specific wavelength. The spectral window corresponds to 1 band in *HyPlant*.

2.4.1.4 Calculation of Vegetation Indices from satellite data

In this study, Sentinel-2 and Sentinel-3 satellites are used to calculate vegetation indices.

Table 12: Sentinel-2A and Sentinel2-B bands characteristics.

band	Sentinel-2A		Sentinel-2B		resolution (m)
	central wavelength (nm)	bandwidth (nm)	Central wavelength (nm)	bandwidth (nm)	
1	442,7	21	442,2	21	60
2	492,4	66	492,1	66	10
3	559,8	36	559	36	10
4	664,6	31	664,9	31	10
5	704,1	15	703,8	16	20
6	740,5	15	739,1	15	20
7	782,8	20	779,7	20	20
8	832,8	106	832,9	106	10
8a	864,7	21	864	22	20
9	945,1	20	943,2	21	60
10	1373,5	31	1376,9	30	60
11	1613,7	91	1610,4	94	20
12	2202,4	175	2185,7	185	20

Table 13: Sentinel 3 OLCI Sensor bands characteristics.

Sentinel 3		
band	central wavelength (nm)	bandwidth (nm)
1	400	15
2	412,50	10
3	442,5	10
4	490	10
5	510	10
6	560	10

7	620	10
8	665	10
9	673.75	7,5
10	681.25	7,5
11	708.75	10
12	753.75	75
13	761.25	2,5
14	764.375	3,75
15	767.5	2,5
16	778.75	15
17	865	20
18	885	10
19	900	10
20	940	20
21	1020	40

As CCI and NIRv have been developed on MODIS bands the bands are shown in table 14.

Table 14: MODIS bands characteristics.

MODIS		
Band	Wavelength (nm)	Resolution (m)
1	620–670	250
2	841–876	250
3	459–479	500
4	545–565	500
5	1230–1250	500
6	1628–1652	500
7	2105–2155	500
8	405–420	1000
9	438–448	1000
10	483–493	1000
11	526–536	1000
12	546–556	1000
13	662–672	1000
14	673–683	1000
15	743–753	1000
16	862–877	1000
17	890–920	1000
18	931–941	1000
19	915–965	1000

Calculation of NDVI

NDVI is calculated from satellite data using Sentinel 2a bands 4, and 8. (see eq. 18)

$$NDVI_{Sentinel-2} = \frac{\rho_{B8} - \rho_{B4}}{\rho_{B8} + \rho_{B4}} \quad (18)$$

Where ρ denotes reflectance. $B4$ denotes band 4 with a central wavelength at 664.6 nm and 32 nm bandwidth, and $B8$ denotes band 8 with a central wavelength at 832.8 nm and 106 nm bandwidth.

	Doc.: Photosynthesis report Version1		
	Date: 27.11.2019	Issue: 2	Revision: 1
	Ref.: ESA Contract No. ESA RFP/3-15506/18/NL/NF		Page: 43 / 69

Calculation of EVI

NDVI is calculated from satellite data using Sentinel 2a bands 2, 4, and 8 (see eq. 19)

$$EVI_{Sentinel-2} = 2.5 \left[\frac{\rho_{B8} - \rho_{B4}}{\rho_{B8} + 6 * \rho_{B4} - 7.5 * \rho_{B2} + 1} \right] \quad (19)$$

Where ρ denotes reflectance. $B2$ denotes band 2 with a central wavelength at 492.4 nm and 66 nm bandwidth, $B4$ denotes band 4 with a central wavelength at 664.6 nm and 32 nm bandwidth, and $B8$ denotes band 8 with a central wavelength at 832.8 nm and 106 nm bandwidth.

Calculation of CCI

CCI was calculated from satellite data using MODIS band 1, and 11 (see eq. 20).

$$CCI_{MODIS} = \frac{\rho_{B11} - \rho_{B1}}{\rho_{B11} + \rho_{B1}} \quad (20)$$

Where ρ denotes reflectance. $B1$ denotes band 1 (620-670 nm), and $B11$ denotes band 11 (526-536 nm).

Accordingly, CCI could be calculated from Sentinel-2A bands 2,3 and 4. Since these bands do not cover exactly the same wavelength range as the bands of MODIS, we propose the following formula (see eq 21).

$$CCI_{Sentinel-2A} = \frac{\left(\frac{\rho_{B2} + \rho_{B3}}{2}\right) - \rho_{B4}}{\left(\frac{\rho_{B2} + \rho_{B3}}{2}\right) + \rho_{B4}} \quad (21)$$

Where ρ denotes reflectance. $B2$ denotes band 2 with a central wavelength at 492.4 nm and 66 nm bandwidth, $B3$ denotes band 3 with a central wavelength at 559.8 nm and 36 nm bandwidth, and $B4$ denotes band 4 with a central wavelength at 664.6 nm and 31 nm bandwidth.

Another option is to use Sentinel-3 bands 5, 6, and 7 from OLCI-sensor. Since these bands do not cover exactly the same wavelength range as the bands of MODIS, we propose the following formula (see eq 21).

$$CCI_{Sentinel-3} = \frac{\rho_{Oa5} - \left(\frac{\rho_{Oa6} + \rho_{Oa7}}{2}\right)}{Oa5 + \left(\frac{\rho_{Oa6} + \rho_{Oa7}}{2}\right)} \quad (21)$$

Where ρ denotes reflectance. $Oa5$ denotes band 5 from OLCI with a central wavelength at 510 nm and 10 nm bandwidth, $Oa6$ denotes band 6 with a central wavelength at 560 nm and 10 nm bandwidth, and $Oa7$ denotes band 7 with a central wavelength at 620 nm and 10 nm bandwidth.

Calculation of NIRv

$$NIRv_{ref_{MODIS}} = \left(\frac{\rho_{B2} - \rho_{B1}}{\rho_{B2} + \rho_{B1}} - C \right) * \rho_{B2} \quad (23)$$

Where C is set to 0.08 (see Badgley et al. 2017). Note that the calculation is based on reflectance values. $B1$ denotes band 1 (620-670 nm) and $B2$ denotes band 2 (841-876 nm).

As equivalent, Sentinel-2A satellite bands 4 and 8 could be used (see eq. 24).

	Doc.: Photosynthesis report Version1		
	Date: 27.11.2019	Issue: 2	Revision: 1
	Ref.: ESA Contract No. ESA RFP/3-15506/18/NL/NF		Page: 44 / 69

$$\text{NIRv_ref}_{\text{Sentinel-2A}} = \left(\frac{\rho_{\text{B8A}} - \rho_{\text{B4}}}{\rho_{\text{B8A}} + \rho_{\text{B4}}} - 0.8 \right) * \rho_{\text{B8A}} \quad (24)$$

Where ρ denotes reflectance. B4 denotes band 4 with a central wavelength at 664.6 nm and 31 nm bandwidth, and B8A denotes band 8A with a central wavelength at 864.7.6 nm and 21 nm bandwidth.

Another option is to use Sentinel-3 bands 6, 7 and 17. Since these bands do not cover exactly the same wavelength range as the bands of MODIS, we propose the following formula (see eq 21).

$$\text{NIRv_ref}_{\text{Sentinel-3}} = \left(\frac{\rho_{\text{Oa17}} - \left(\frac{\rho_{\text{Oa6}} + \rho_{\text{Oa7}}}{2} \right)}{\rho_{\text{Oa17}} + \left(\frac{\rho_{\text{Oa6}} + \rho_{\text{Oa7}}}{2} \right)} - 0.8 \right) * \rho_{\text{Oa17}} \quad (24)$$

Where ρ denotes reflectance. Oa6 denotes band 6 with a central wavelength at 560 nm and 10 nm bandwidth, Oa7 denotes band 7 with a central wavelength at 620 nm and 10 nm bandwidth, and Oa17 denotes band 17 with a central wavelength at 865 nm and 20 nm bandwidth.

2.4.2 Calculation of Sun-Induced-Fluorescence Products

Retrieval of sun-induced fluorescence from HyPlant data

To retrieve F values at 760 nm (F_{760}) and 687 nm (F_{687}) from data collected by FLUO module of *HyPlant*, two different retrieval methods were applied - iFLD (Improved Fraunhofer Line Discrimination) method and SFM (Spectral Fitting Method), more in detail described in the following paragraphs.

Improved Fraunhofer Line Discrimination (iFLD)

The improved Fraunhofer Line Discrimination (iFLD) used here, is derived from the Fraunhofer Line Depth (FLD) principle and a further modification of the cFLD, Sun-induced fluorescence retrieval from airborne hyperspectral imaging spectrometer another variation of FLD (Meroni et al, 2009). As described by Damm et al., 2015, FLD relies on the use of atmospheric absorption bands, the so-called Fraunhofer lines, characterized by lower incident light compared to wavelength regions outside of this bands. Subsequently, the infilling of F can be quantified, separating the F signal from reflected radiance by using radiance measurements inside and outside the O₂-A absorption band around 760 nm and the O₂-B absorption band at 687 nm. iFLD was the modification of FLD used in this study, with an additional semi-empiric correction applied for each scan line across track (Damm et al., 2015). Therefore, reference surfaces (e.g. bare soils) are employed, free of any F signal, for adjusting the upward transmittance. Furthermore, atmospheric radiative transfer models, such as MODTRAN-5 (Berk et al., 2005) and the MODTRAN interrogation technique introduced by Verhoef and Bach, 2003, were used for correcting atmospheric influences.

Spectral Fitting Method (SFM)

The Spectral Fitting Method (SFM) has been developed further based on the previous work by Meroni et al., 2010; Mazzoni et al., 2012 and Cogliati et al., 2015. The advantage of this approach is that it does not require areas free of vegetation within the image scene for retrieving F, as it relies on a physically based approach. This is a crucial advantage, making SFM approach a suitable retrieval method for the future FLEX mission (Kraft et al., 2017). The SFM approach is based on coupled surface atmosphere forward model that uses the atmospheric MODTRAN code. The next step is decoupling the F signal and surface reflected radiance from the total-at-sensor signal, using mathematical functions to model canopy reflectance and F spectra at the different wavelengths. Exploiting the full set of spectral bands

	Doc.: Photosynthesis report Version1		
	Date: 27.11.2019	Issue: 2	Revision: 1
	Ref.: ESA Contract No. ESA RFP/3-15506/18/NL/NF		Page: 45 / 69

provided by *HyPlant* sensor the full fluorescence spectrum in the range from 670 nm to 780 nm can be derived (Cogliati et al., 2015; Cogliati et al., 2018), increasing the information content compared to iFLD.

2.4.3 Calculation of GPP from continuous and stationary flux measurements

Selhausen, Germany

Half-hourly values of GPP was estimated from the NEE measurements by using a daytime data-based flux-partitioning algorithm after Lasslop et al. (2010), implemented in the gap-filling and source partitioning software REddyProc (REddyProc Team, 2014). This approach models GPP with a rectangular hyperbolic light-response curve with additional consideration of the vapor pressure deficit limitation of photosynthesis. Data gaps in the time series of the meteorological driver variables (taken from the climate station of the Selhausen site) required for modelling GPP were filled before partitioning with a variant of the data interpolating empirical orthogonal functions method (Beckers and Rixen, 2003; Graf, 2017).

Lincoln-Nebraska, USA

The Nebraska flux measurements are headed by Dr. Andy Suyker, who follows standard Ameriflux protocols and all the data are eventually available via Ameriflux.

2.4.4 Calculation of carbon and water fluxes form airborne concentration measurements

Standard flows already exist ($w'c'$ with 10 Hz versus 60 s moving averages, where c stands for CO_2 , H_2O and heat). A new method is being developed with which the footprints can also be estimated. From this, a more exact statement can be made, from which fields the water vapour and the sensible heat came, and/or where the CO_2 was absorbed.

Here, the data are provided after the post-processing of the raw data (level 1) to synchronized, calibrated data (level 2) of the in-situ measurements near Grosseto in June and July 2018. Since the focus was and will be on 'fluxing' (calculating turbulent fluxes of H_2O and CO_2 from and to the vegetation), the focus was not so much on the absolute values (accuracy), but a good temporal resolution and well synchronized fast measurements of the correct amplitudes (precision) at 10 Hz within a time scale of a few minutes.

Therefore, we achieved a data set from twelve days during three episodes with different phenology (development of the vegetation), where the in-situ fluxes can be compared with the characteristics gained from remote sensing by satellites and other aircraft.

Several improvements have been introduced for the third IOP, where a 'Los Gatos ultra-portable Greenhouse Gas Analyzer' (LG UGGA) was installed, which added (slow) CH_4 and also allowed to improve the absolute calibration of CO_2 and H_2O even for the previous days. Further, a fluorescence spectrometer from FZJ was installed for testing.

All the calibrations including accurate wind components were achieved by iterative optimizations of dependent parameters.

During the post-processing, up to 84 primary (raw) parameters (including LG UGGA) were treated, leading to a total of 175 parameters per flight. Many of them have strong interactions (as e.g. the density and hence the wind from pressure, temperature, and even humidity, or some interferences of IRCO_2 with IRH_2O and aer03). Others needed careful adjustments like the three-dimensional flow towards the five-hole-probe, resulting in 3-d wind after subtracting the movement of the aircraft.

	Doc.: Photosynthesis report Version1		
	Date: 27.11.2019	Issue: 2	Revision: 1
	Ref.: ESA Contract No. ESA RFP/3-15506/18/NL/NF		Page: 46 / 69

The output format MetAir_18mdd_1Hz.dat is the first example of data. It is a tab-delimited ASCII file that can easily be imported in Excel or other programs for inspecting the data. The 1-Hz-temporal resolution is sufficient for most applications.

3 Tentative Results and Discussion

3.1 Results from Selhausen, Germany

3.1.1 Seasonal dynamics of top-of-canopy measurements

Data are shown from mid to end of June 2018 measured in a winter wheat field near Selhausen. These were taken from the FloX, the EC Tower and the ICOS Tower, which are located in the middle of the field.

In Germany, the temperatures for June are between 10 and 20°C in average. For June 2018, the average temperatures measured are higher.

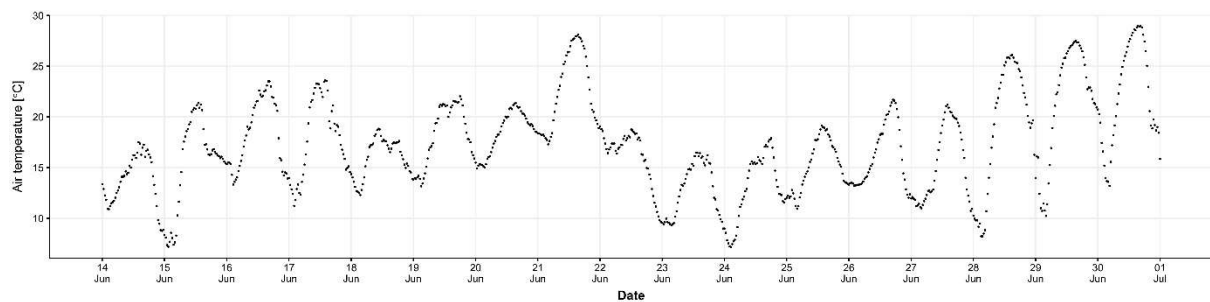


Figure 19: Air temperature from June, 14th to June, 31st in 2018 measured from ICOS Tower in a winter wheat field near Selhausen, Germany.

The PAR data from the Flox show that the lighting conditions were mostly variable, except on 20th June when they appear stable and from 26th June to 1st July.

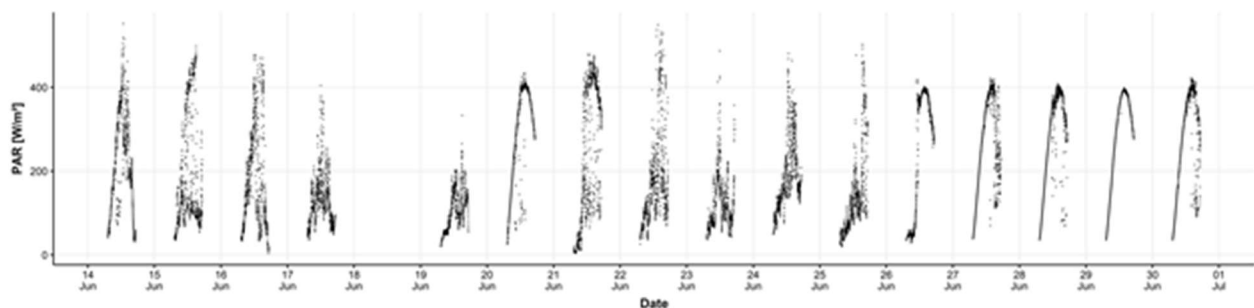


Figure 20: PAR from June, 14th to June, 31st in 2018 measured by FloX in a winter wheat field near Selhausen, Germany.

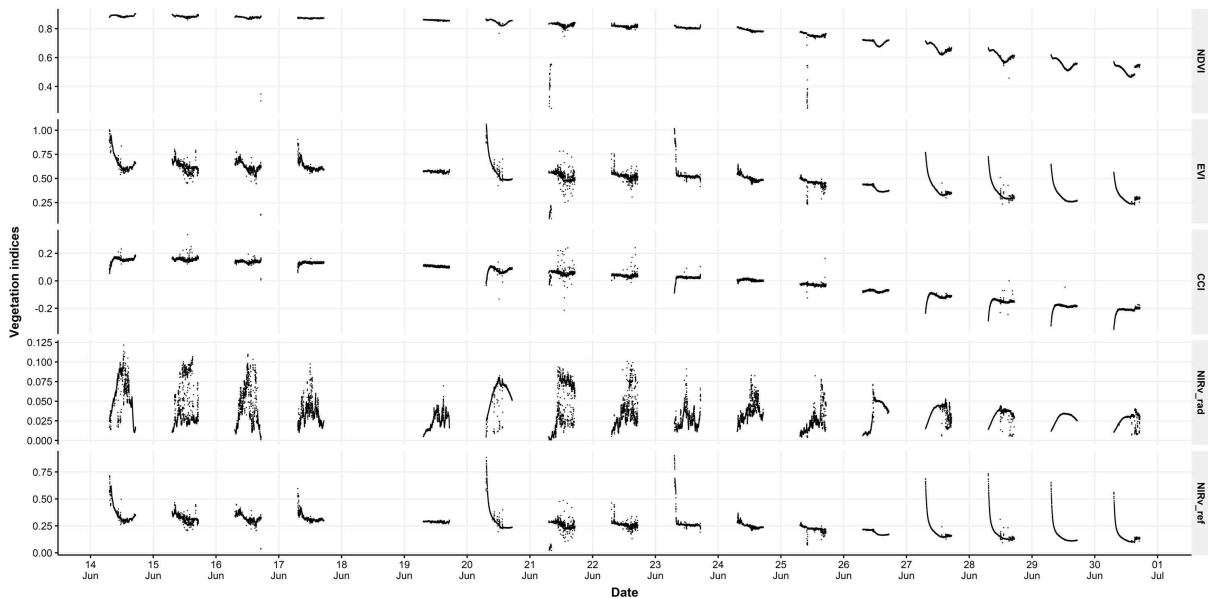


Figure 21: Vegetation indices processed from a FloX in a winter wheat field near Selhausen, Germany. Measured in the period from 14th of June to 31st of June in 2018. From top to bottom: NDVI, EVI, CCI, NIRv_ref (NDVI*R800), NIRv_rad (NDVI*L800).

The absolute values of the vegetation indices (VI's) decrease in the period from mid to end of June. On days with quite stable weather conditions, a strong increase or decrease is visible at the beginning of the day for all VIs except NDVI. This is probably due to shadow effects of the canopy. With EVI this is due to the consideration of the blue wavelength range. But also the CCI and the NIRv calculations with the reflection or radiance at 800 nm take this into effect.

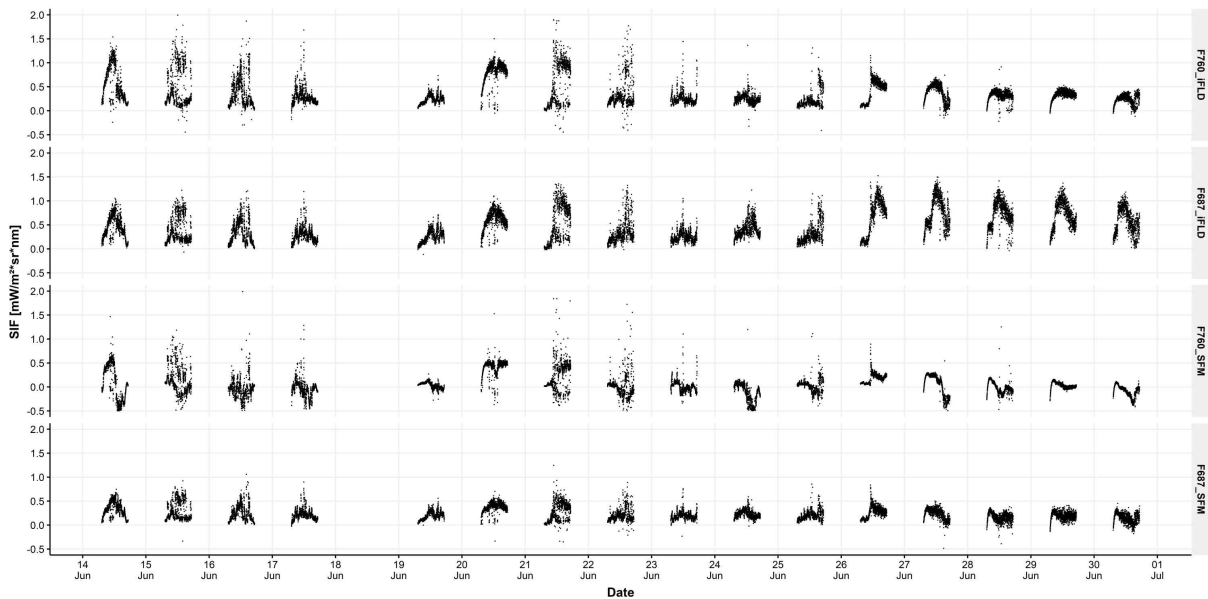


Figure 22: SIF processed from a FloX in a winter wheat field near Selhausen, Germany. Measured in the period from 14th June to 31st June in 2018. From top to bottom: F₇₆₀ retrieved from iFLD, F₆₈₇ retrieved from iFLD, F₇₆₀ retrieved from SFM, F₆₈₇ retrieved from SFM.

The SIF products of both retrievals show significantly more variability over the day than any VI's previously shown. A connection with the PAR values can be guessed, a normalization with these and calculation of SIFyield will therefore be the next step.

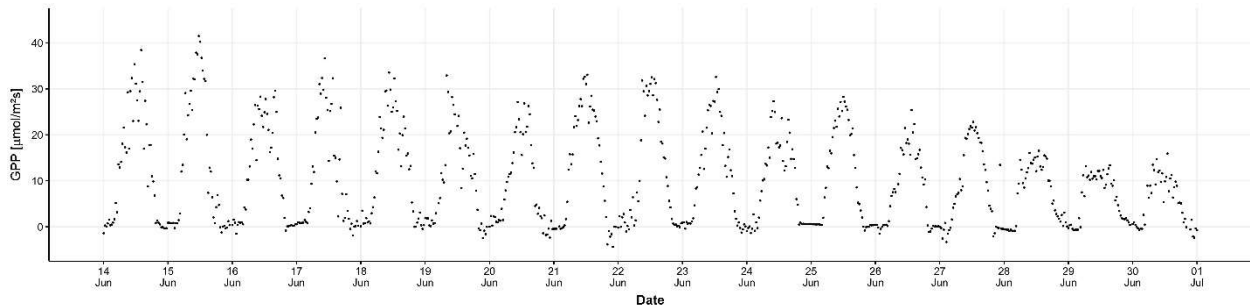


Figure 23: GPP (based on Reichstein-method) from June, 14th to June, 31st 2018 measured from the EC001 Tower in a winter wheat field near Selhausen, Germany.

The absolute GPP values decrease towards the end of the month, which will be due to the reduced photosynthesis activity of the increasingly mature winter wheat (Figure 25). On July 16th, the field was harvested.

3.1.2 Diurnal dynamics of top-of-canopy measurements

Data from 26th of June are displayed here as examples. On this day, in addition to the ground measurements, data are available from two overflights with the *HyPlant* sensor at 1800 and 600 m altitude in TR32 and SEL flight patterns. The SEL flight pattern is covered by two airlines. Figure 26 shows a true colour image and the derived vegetation indices of the Selhausen area with the winter wheat field in the centre.

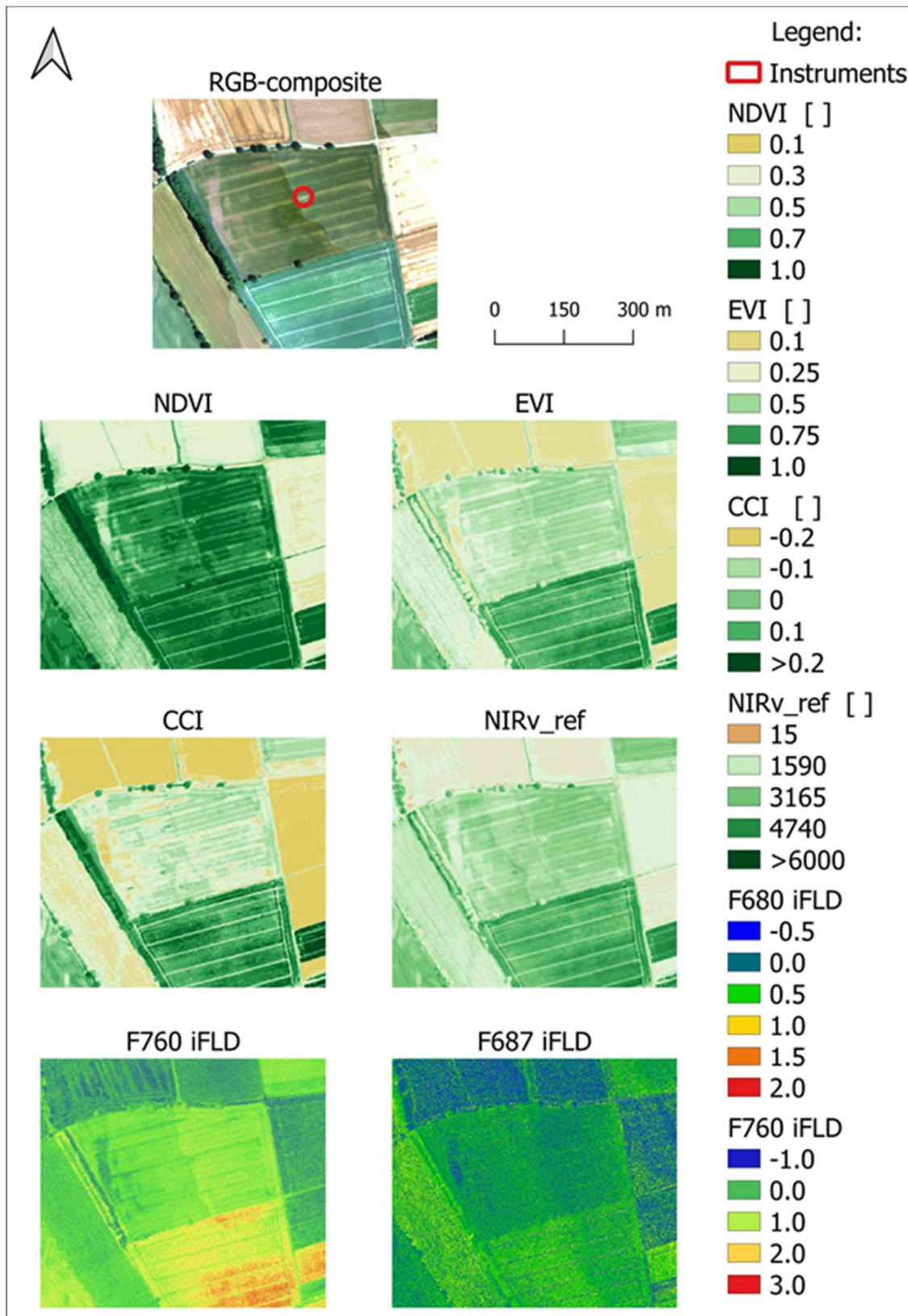


Figure 24: Maps showing the area around the EC-Tower, the ICOS Station, FloX and SIFsSys ('Instruments': marked with red circle) in a winter wheat field near Selhausen. The data originate from the *HyPlant* overflight on 26th of June 2018 (flight pattern SEL, 600 m altitude).

The winter wheat field with some trees at the field's edge and tractor tracks running through the field is not homogeneous, but the part in the west seems less green than the part in the east. The region is characterized by a paleo lithic riverbed, which is still recognizable today by the different water retention capacities of the soil (Simmer et al, 2015). These patterns can be seen on the maps. The vegetation-indices give different values for the winter wheat field, whereby the heterogeneity of the field, visible in the true-colour image, is given as a very similar pattern.

26th of June 2018 was an almost cloudless day with an average temperature of around 18 °C during the day (Figure 27).

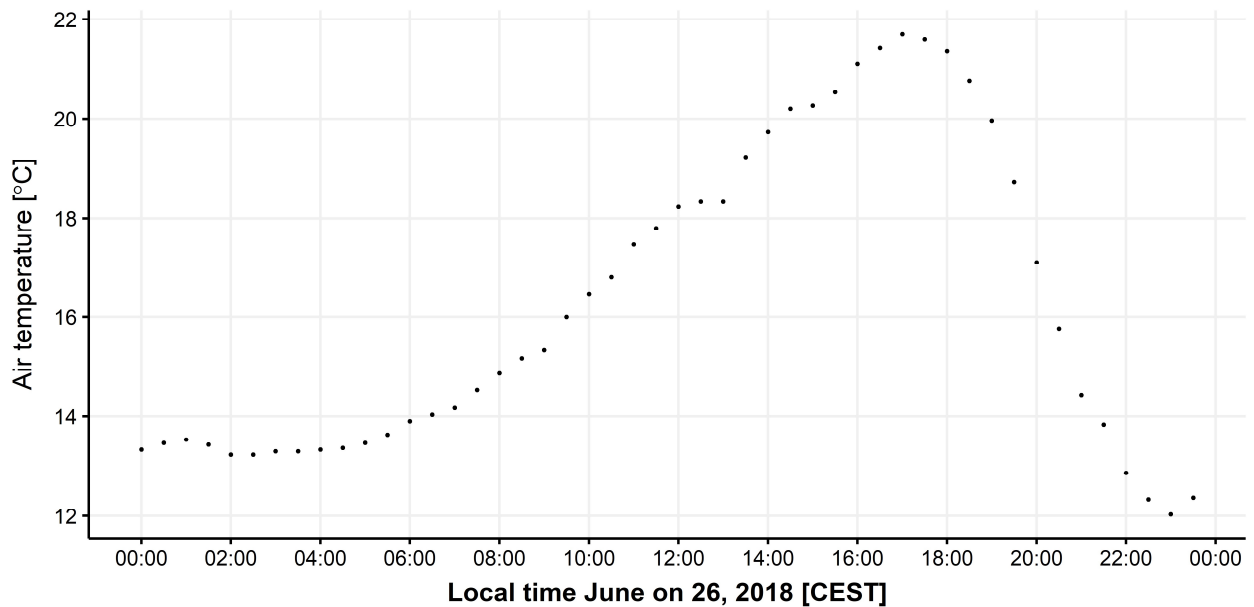


Figure 25: Air temperature from June, 26 2018 measured from ICOS Tower in a winter wheat field near Selhausen, Germany.

Figure 28 shows that the light conditions changed between 11 and 12 o'clock, which is probably due to some clouds.

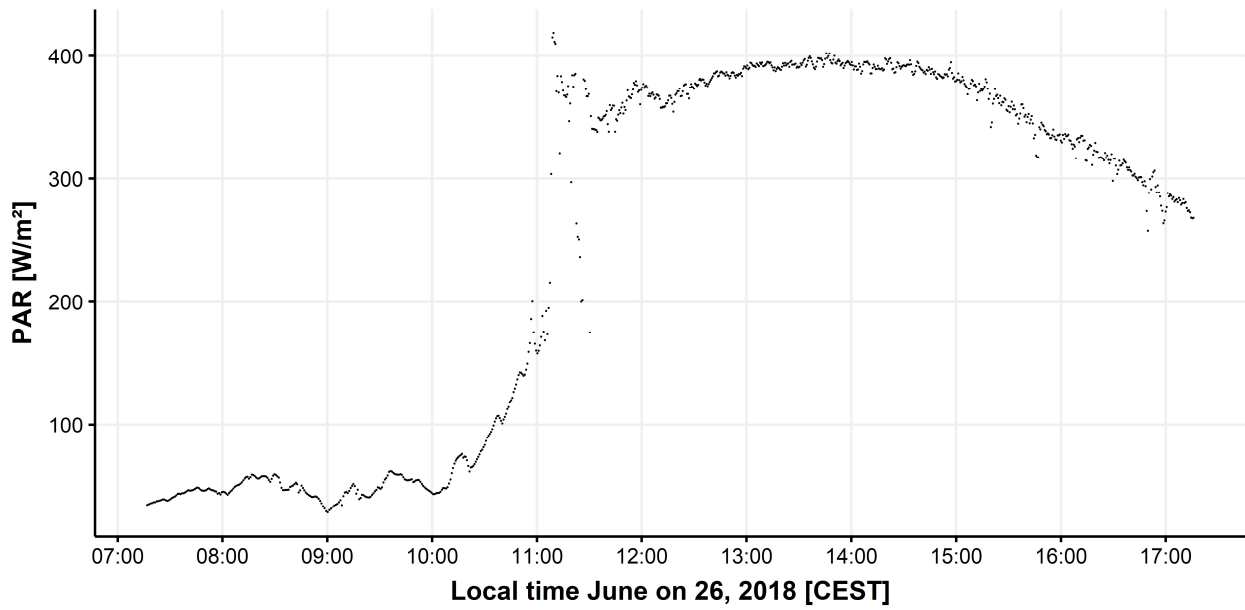


Figure 26: PAR from June, 26th in 2018 measured by FloX in a winter wheat field near Selhausen, Germany.

Figure 29 shows the VI's processed from the FloX: NDVI, EVI, CCI, NIRv based on NDVI*R800 and based on NDVI*L800. (Rows 1 to 5)

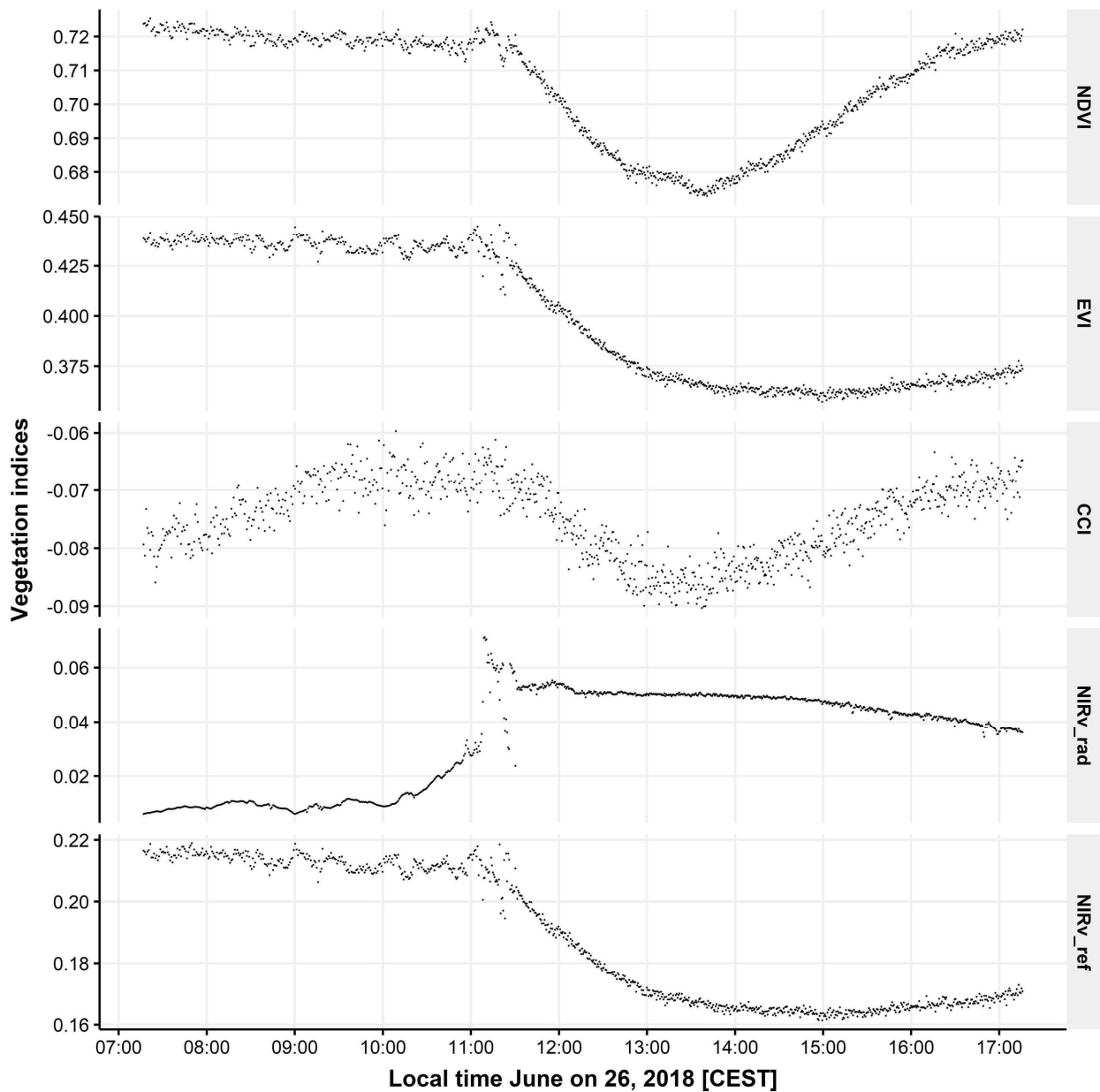


Figure 27: Vegetation indices processed from a FloX in a winter wheat field near Selhausen, Germany. Measured on June, 26th in 2018. From top to bottom: NDVI, EVI, CCI, NIRv_ref (NDVI*R800), NIRv_rad (NDVI*L800).

Until noon the values of all indices are quite stable, then they drop for all indices except the NIRv_rad. All indices show a strong increase / decrease in daytime cycling during the changing light conditions between 10 and 12 o'clock.

Figure 30 shows the SIF values of F_{760} and F_{687} obtained from the FloX using both the iFLD method (rows 1 and 2) and the SFM method (rows 3 and 4).

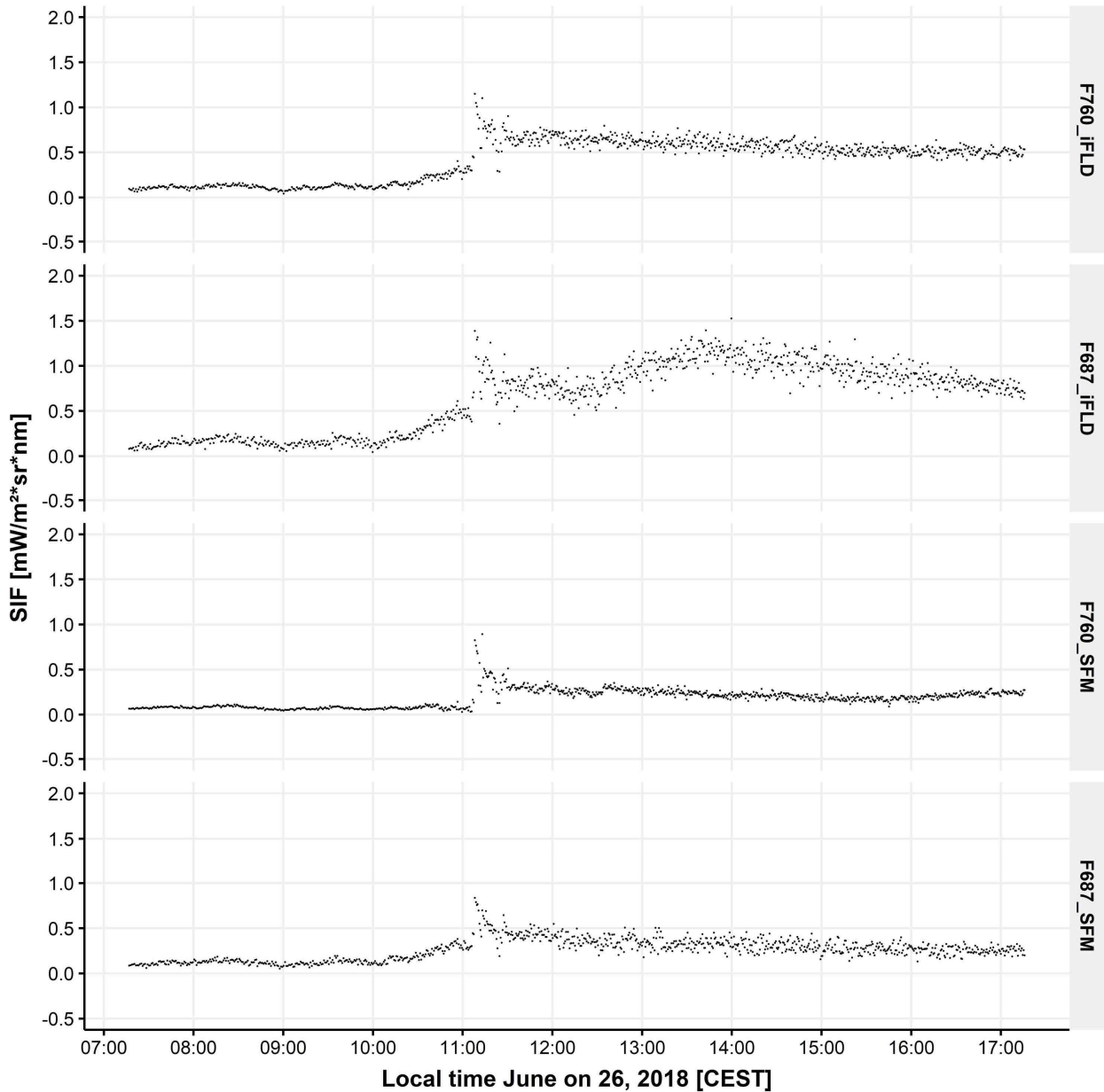


Figure 28: SIF processed from a FloX in a winter wheat field near Selhausen, Germany. Measured on June, 26th in 2018. From top to bottom: F_{760} retrieved from iFLD, F_{687} retrieved from iFLD, F_{760} retrieved from SFM, F_{687} retrieved from SFM.

The SIF values are also changing exactly at the time of these changing lighting conditions, independent of the retrieval method. It can also be seen that the F_{687} product retrieved with the iFLD generally deviates more than the one retrieved with the SFM.

The following figures show the Water Vapour pressure deficit and GPP from EC Tower (Figure 31 and 32).

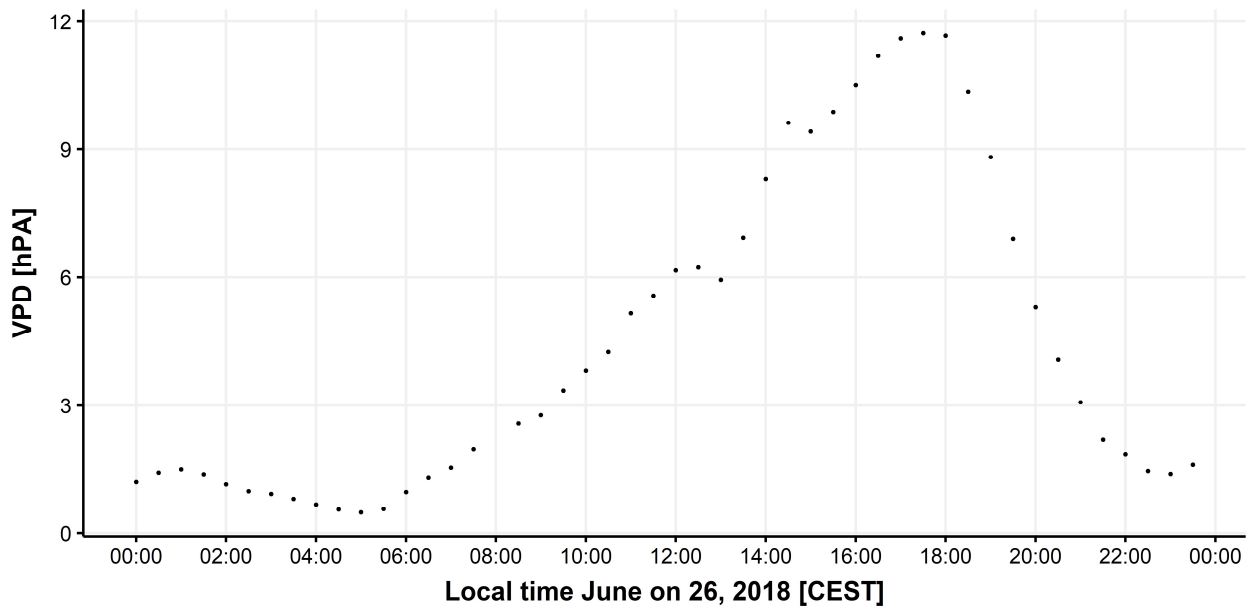


Figure 29: Water Vapour pressure deficit (VPD) from June, 26th in 2018 measured from the EC001 Tower in a winter wheat field near Selhausen, Germany.

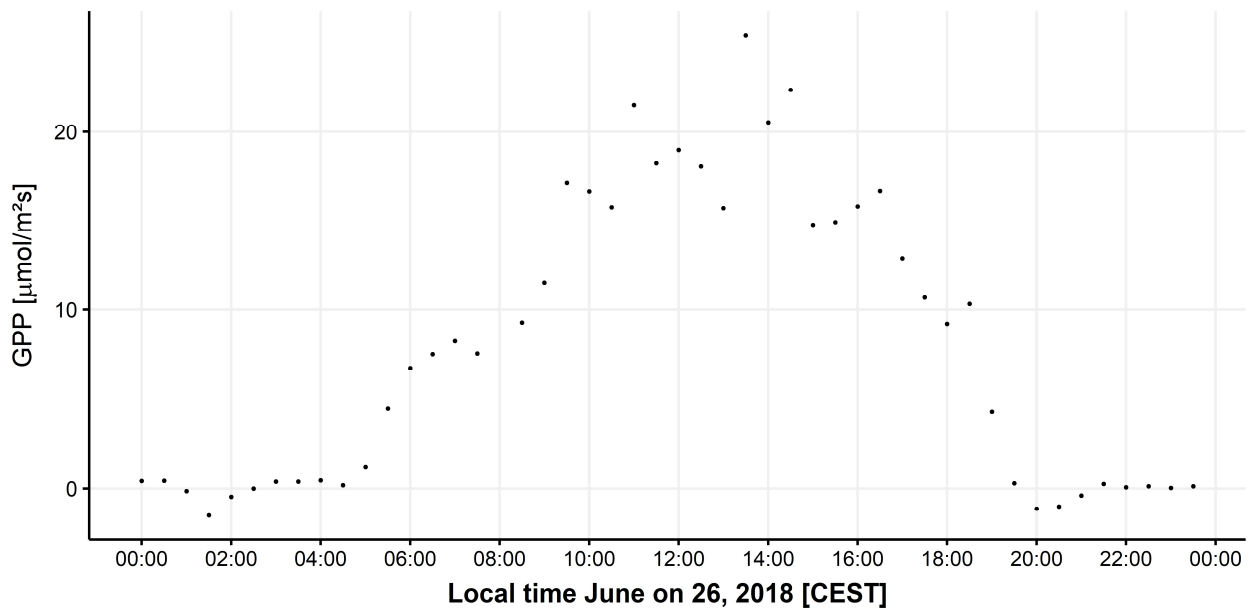


Figure 30: GPP (based on Reichstein-method) from June, 26th in 2018 measured from the EC001 Tower in a winter wheat field near Selhausen, Germany.

The course of the day of the GPP does not show this light ratio change between 10 and 12 o'clock as an anomaly in the course of the day, as it was visible with the VI's and SIF.

3.2 Results from Majadas, Spain

3.2.1 2018 Heatwave in Majadas, Spain

3.2.1.1 Seasonal dynamics

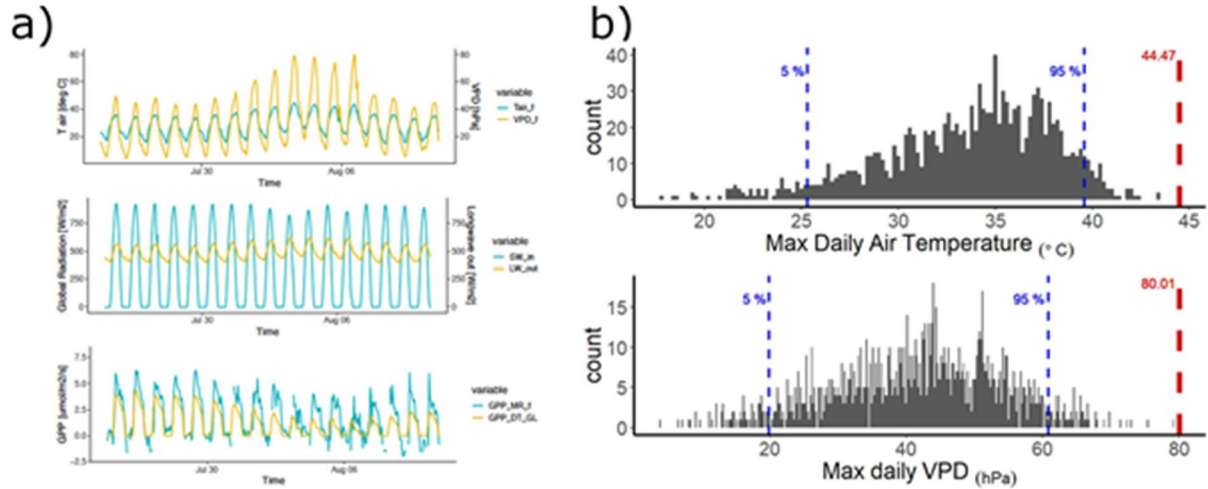


Figure 31: Air temperature (T_{air}), Global radiation and gross primary production (GPP) during the heatwave of 2018 a). Comparison of the maximum air temperature (44.47 °C) and maximum VPD (80.01 hPa) during the 2018 heatwave with the maximum daily temperature and maximum daily VPD from 2004 to 2018 in the months of June, July and August in b). Maximum air temperature and VPD are represented with red dashed lines and the 95 % and 5 % of the distribution of maximum daily temperature and VPD are indicated with blue dashed lines.

The summer of 2018 was characterized by a heatwave, with unusually high air temperatures (T_{air}) and vapour pressure deficit (VPD) that affected most of Europe resulting in significant reduction in LAI and widespread plant mortality (Albergel *et al.*, 2019). Also Spain was affected. In Figure 33a, it is possible to see an increase in both T_{air} and decrease in GPP during the heatwave window (Aug 1st -Aug 7th) at the experimental site of Majadas, Spain. Maximum T_{air} registered was 44.47°C and the maximum VPD was 80.01 hPa (Figure 33b). Both the maximum, T_{air} and VPD were the highest ever registered in the last 12 years at Majadas.

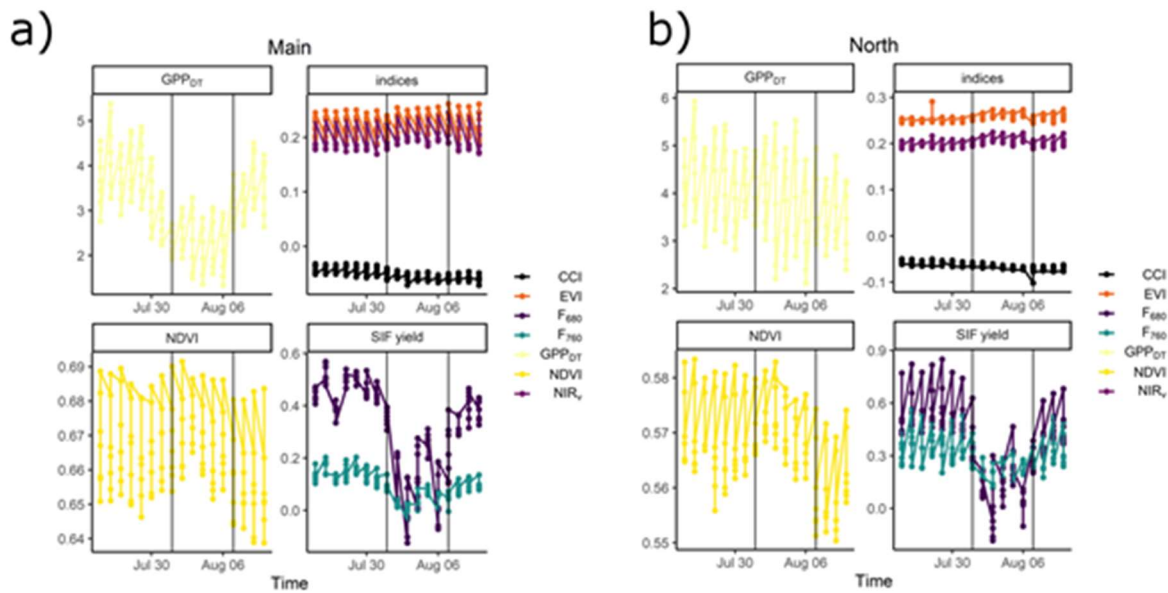


Figure 32: Gross primary production from day time partitioning (GPP_{DT}), normalized difference vegetation index (NDVI), Chlorophyll Carotenoid index (CCI), enhanced vegetation index (EVI), Near-infrared reflectance of terrestrial vegetation (NIR_v), sun-induced fluorescence at 760 nm (F_{760}) and sun-induced fluorescence at 680 nm (F_{680}) during the 2018 heatwave in the control tower a) and nitrogen fertilized tower b). F_{760} , F_{680} and indices are from an evergreen *Q. ilex* tree, where the GPP is from the tall eddy covariance EC towers in the control and nitrogen fertilized treatment, respectively. Black lines represent the start and the end of the heatwave.

GPP from day time partitioning (GPP_{DT}), F_{760} and F_{680} presented significant reduction during the heatwave, whereas indices such as CCI, EVI, NDVI and NIR_v were not significantly altered (Figure 34a,b). As the heatwave lasted only 7 days and the CCI index, which is used to track change in chlorophyll content, was not affected by the extreme event, is possible to conclude that no chlorophyll degradation took place during the heatwave, and that changes in F_{760} and F_{680} are mostly due to physiological regulation rather than changes in leaf or canopy structure. Interestingly, it seems that at both the control tower (Figure 34a) and the nitrogen fertilized tower (Figure 34b), the F_{680} was more affected by the extreme temperature and VPD in comparison with F_{760} , suggesting that the two peaks of SIF respond differently to stress and carry different information.

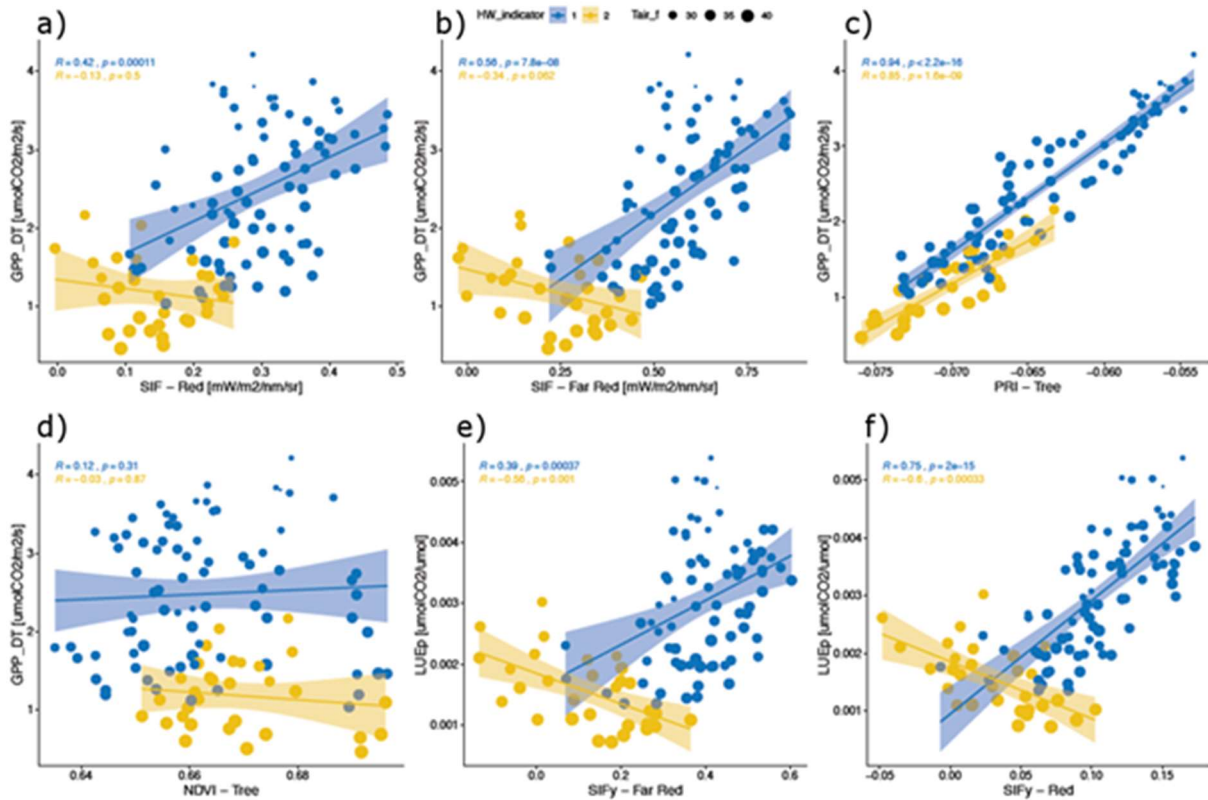


Figure 33: Relationship between Gross primary production from day time partitioning (GPP_{DT}) and sun-induced fluorescence (SIF) at 680 nm (SIF-Red) in a), Relationship between GPP_{DT} and SIF at 760 nm (SIF - Far Red) in b) GPP_{DT} and photochemical reflectance index (PRI) in c), GPP_{DT} and NDVI in d), relationship between light use efficiency of photosynthesis (LUE_p), calculated as GPP/PAR and fluorescence yield at 760 nm (SIFy - Far red) calculated as F_{760}/PAR in e) and relationship between LUE_p and fluorescence yield at 680 nm (SIFy - Red) calculated as F_{680}/PAR f), at the nitrogen fertilized tower in Majadas. Yellow dots indicate the heat wave period whereas blue dots indicate the days before and after the heatwave. GPP and LUE_p are from the tall eddy covariance (EC) tower at the nitrogen fertilized treatment, whereas SIF -Red , SIF -Far Red, SIFy, NDVI and PRI are from one evergreen Q. ilex tree at the nitrogen fertilized treatment.

The relationship between GPP_{DT} and F_{680} (Figure 35a) and GPP and F_{760} (Figure 35b) is positive and significant before and after the heatwave (blue dots in Figure 35), but breaks down during the heatwave period (yellow dots). When normalizing by PAR both the GPP and the SIF, the contrast between the heatwave and the days before and after becomes even clearer. In Figure 35e and Figure 35f, the relationship between the light use efficiency of photosynthesis (LUE_p) and F_{760}/PAR , and LUE_p and F_{680}/PAR becomes significantly negative during the heatwave ($p < 0.01$ in both cases). It is possible that in response to the extreme events, plants respond by shifting the allocation of absorbed PAR preferably to SIF that is reduced during the heatwave, but to a lesser extent compared to GPP. The best predictor of GPP during the heatwave was PRI (Figure 35c), indicating that during a heatwave the photosynthetic activity is highly controlled by xanthophyll cycle, which is tracked by PRI. Finally, NDVI fails to predict GPP both during the heatwave and in the days before and after (Figure 35d).

3.3 Results from Mead, USA

3.3.1 Seasonal dynamics

2018 was a relatively wet year in Nebraska; consequently only minor stress events were seen. Nevertheless, data collected from the D-FLOX over the growing season provided a preliminary

assessment of the degree to which SIF and GPP were controlled by structure (Absorbed Photosynthetically Active Radiation, APAR) and stress (light-use efficiency, LUE). Since both SIF and GPP seem to respond similarly to periods of varying LUE (red arrows in Figure 36), the resulting SIF-GPP relationship is strong (Figure 36), supporting the use of SIF as an indicator of photosynthetic rate (GPP).

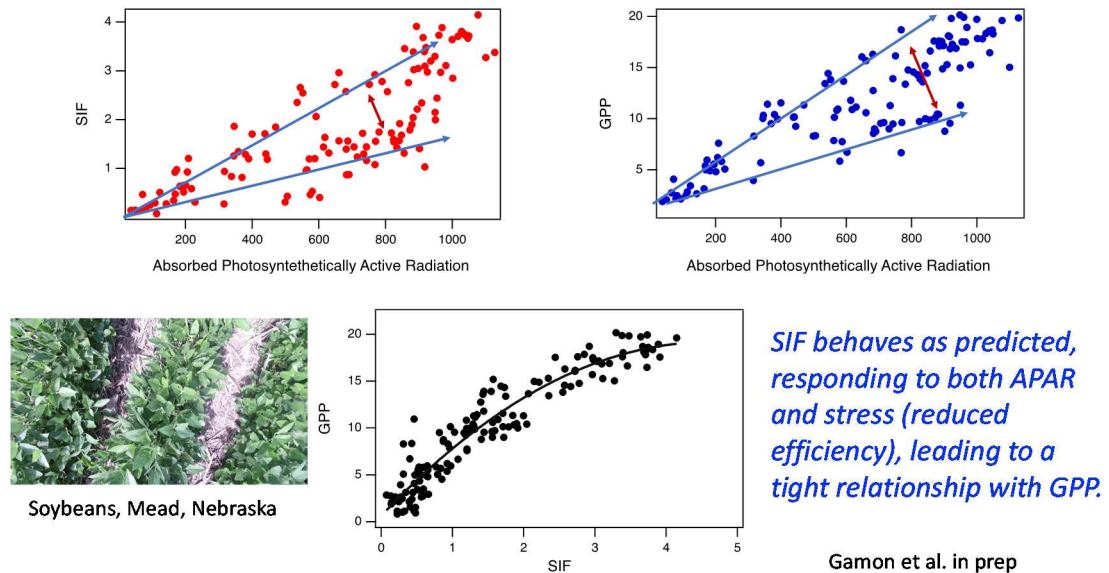


Figure 34: SIF or GPP versus absorbed photosynthetically active radiation and GPP versus SIF.

Analysis of the seasonal patterns of GPP, SIF, and NDVI show a close relationship between SIF and GPP (red and blue lines respectively, Figure 37). Both GPP and SIF captured short-term variation in APAR and LUE (Figure 36), seen as the coincident responses to day-to-day conditions (Figure 37). On the other hand, NDVI failed to capture these day-to-day changes in GPP (black line, Figure 37).

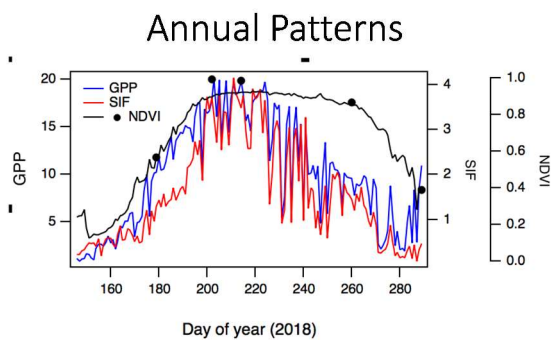


Figure 35: Fluorescence (SIF) closely tracks photosynthesis at all temporal scales.

3.3.2 Diurnal dynamics

Diurnal comparison between the D-Flox SIF and GPP generally show good agreement (Figure 38) further supporting the use of SIF as an optical metric of GPP.

Daily Patterns

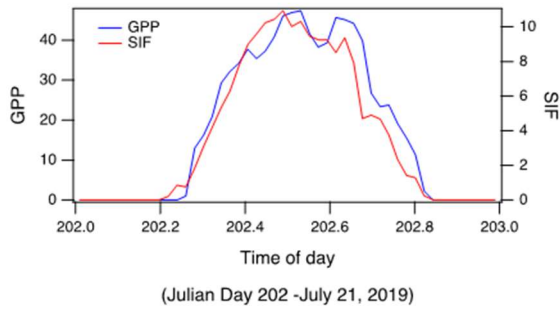


Figure 36: Fluorescence (SIF) closely tracks photosynthesis at all temporal scales.

3.3.3 Aircraft SIF measurements

A comparison of the D-Flox SIF to the aircraft SIF show broadly similar seasonal trends, with periods of disagreement (Figure 39), possibly due to the flights occurring at different times of day (having different illumination and atmospheric conditions). Further analyses are underway to better understand the reasons for this variable agreement between aircraft and ground SIF values.

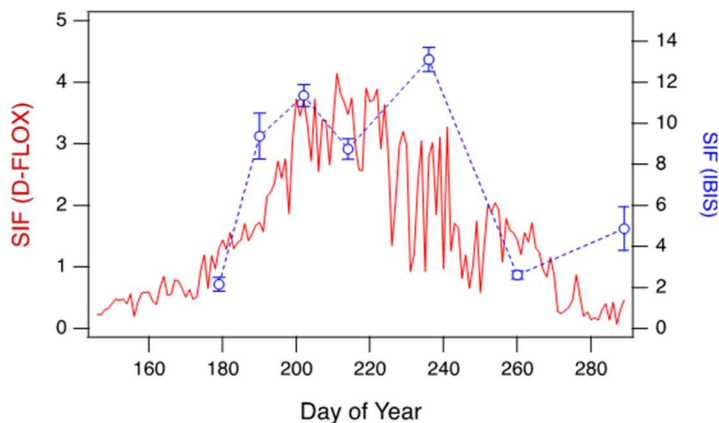


Figure 37: Comparison of D-FloX to IBIS (preliminary)

Aircraft SIF data generally show spatial patterns with more detail than NDVI (Figure 40), suggesting that SIF can reveal patterns in productivity that are not always visible to conventional greenness indices (e.g. NDVI).

Spatial patterns of SIF vs. NDVI



CSP3 – Soybeans, July 21, 2018

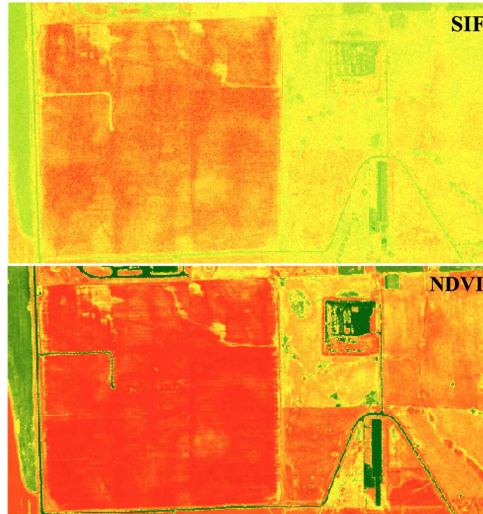
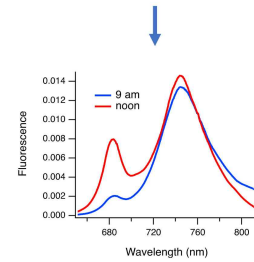
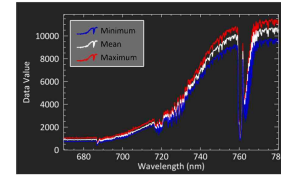


Figure: Hamed Gholizadeh



Gamon et al (in prep)

Figure 38: Spatial patterns of SIF versus NDVI.

3.4 Results from Grosseto, Italy

The data from Grosseto, Italy will be analysed after the analysis of the Selhausen data. The same processing approach will be applied for the *HyPlant*, FloX and Satellite data as it was for the measurements in Selhausen.

3.5 Fluxes

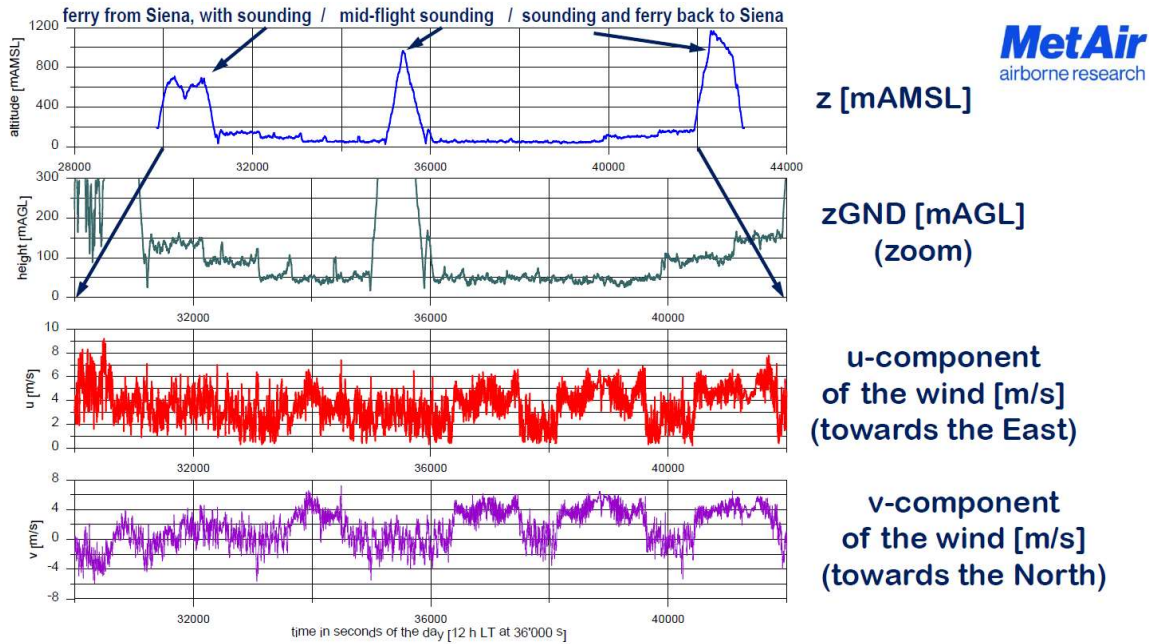


Figure 39: Preliminary results of the flight from June 19th 2018 over Grosseto, Italy. Shown are 1 Hz data, averaged from 10 Hz original resolution.

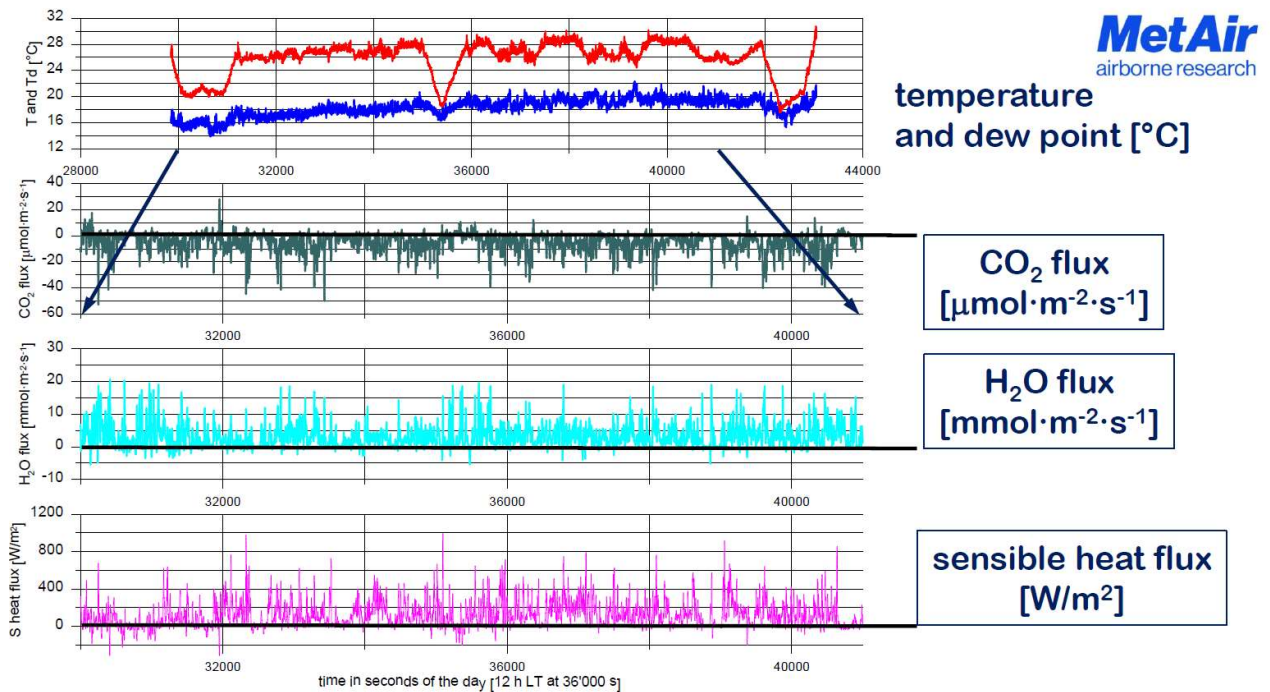


Figure 40: Preliminary results of the flight from June 19th 2018 over Grosseto, Italy. Shown are fluxes from 10 Hz on moving averages of 60 s.

	Doc.: Photosynthesis report Version1		
	Date: 27.11.2019	Issue: 2	Revision: 1
	Ref.: ESA Contract No. ESA RFP/3-15506/18/NL/NF		Page: 63 / 69

4 Discussion

This is a living document. Therefore, this section with first conclusions drawn from results can be listed here as preliminary and may be changed/further developed.

SIF represents an invaluable tool to track and predict photosynthesis and transpiration (Shan *et al.*, 2019), which has been successfully applied at both canopy (Damm *et al.*, 2010;) and global scale (Guanter *et al.*, 2014). However, it is not enough understood about the influence of stress events such as extreme temperature or drought on the relationship between GPP- F_{760} . In this work we show by analysing the 2018 heatwave in Spain that F_{760} and F_{680} are strongly affected by the heatwave and that GPP and SIF respond differently to extreme temperature. During the heatwave the usually positive relationship between GPP and F_{760} becomes negative, highlighting the non-linear nature of the relationship between GPP and F_{760} . The two peaks of SIF (F_{760} and F_{680}) reacted differently to the heatwave, indicating that the two peaks of SIF carry out different information and can be used together to understand vegetation stress. Finally, PRI was the best predictor of GPP during the heatwave, which indicate that photosynthetic activity was highly controlled by heat dissipation processes. These results suggest that including PRI in an empirical model together with F_{760} might improve GPP prediction, especially during stress conditions.

	Doc.: Photosynthesis report Version1		
	Date: 27.11.2019	Issue: 2	Revision: 1
	Ref.: ESA Contract No. ESA RFP/3-15506/18/NL/NF		Page: 64 / 69

5 References

The following literature is relevant for this project. Literature cited in this document is marked with an asterisk (*).

Aasen Helge, Burkart Andreas, Bolten Andreas, Bareth Georg (2015). Generating 3D hyperspectral information with lightweight UAV snapshot cameras for vegetation monitoring: From camera calibration to quality assurance, *ISPRS Journal of Photogrammetry and Remote Sensing*, Volume 108, Pages 245-259.

Albergel C, Dutra E, Bonan B, Zheng Y, Munier S, Balsamo G, de Rosnay P, Muñoz-Sabater J, Calvet J-C. 2019. Monitoring and forecasting the impact of the 2018 summer heatwave on vegetation. *Remote Sensing* 11(5): 520. *

Badgley, G., Field, C. B., & Berry, J. A. (2017). Canopy near-infrared reflectance and terrestrial photosynthesis. *Science Advances*, 3(3). *

Beckers JM, Rixen M (2003) EOF calculations and data filling from incomplete oceanographic datasets. *J Atmos Ocean Technol* 20(12):1839–1856*

Berk, A., Anderson, G. P., Acharya, P. K., Bernstein, L. S., Muratov, L., Lee, J., Fox, M., & Lockwood, R. B. (2005, June). MODTRAN 5: a reformulated atmospheric band model with auxiliary species and practical multiple scattering options: update. In *Algorithms and technologies for multispectral, hyperspectral, and ultraspectral imagery XI* (Vol. 5806, pp. 662-668). International Society for Optics and Photonics. *

Brosy C, Krampf K, Zeeman M, Wolf B, Junkermann W, Schäfer K, Emeis S, Kunstmann H (2017) Simultaneous multicopter-based air sampling and sensing of meteorological variables. *Atmospheric Measurement Techniques* 10(8).

Burkart A, Aasen H, Alonso L, Menz G, Bareth G, Rascher U. (2015) Angular dependency of hyperspectral measurements over wheat characterized by a novel UAV based goniometer. *Remote Sensing* 7:725-746. *

Burkart A, Schickling A, Cendrero Mateo MP, Wrobel T, Rossini M, Cogliati S, Julitta T, Rascher U. (2015) A method for uncertainty assessment of passive sun-induced chlorophyll fluorescence retrieval by using an infrared reference light. *IEEE Sensors* 15:4603-4611. *

Cogliati, S., Rossini, M., Julitta, T., Meroni, M., Schickling, A., Burkart, A., Pinto, F., Rascher, U. and Colombo, R., 2015. Continuous and long-term measurements of reflectance and sun-induced chlorophyll fluorescence by using novel automated field spectroscopy systems. *Remote sensing of environment*, 164, pp.270-281. *

Cogliati, S., Verhoef, W., Kraft, S., Sabater, N., Alonso, L., Vicent, J., Moreno, J. & Colombo, R. (2015). Retrieval of sun-induced fluorescence using advanced spectral fitting methods. *Remote sensing of environment*, 169, 344-357. *

Cogliati, S., Colombo, R., Celesti, M., Tagliabue, G., Rascher, U., Schickling, Rademske, P., Alonso, A., Sabater, N., Schuettemeyer, D. & Drusch, M. (2018, July). Red and Far-Red Fluorescence Emission Retrieval from Airborne High-Resolution Spectra Collected by the Hyplant-Fluo Sensor. In *IGARSS 018-2018 IEEE International Geoscience and Remote Sensing Symposium* (pp. 3935-3938). IEEE. *

	Doc.: Photosynthesis report Version1		
	Date: 27.11.2019	Issue: 2	Revision: 1
	Ref.: ESA Contract No. ESA RFP/3-15506/18/NL/NF		Page: 65 / 69

Damm A, Elbers J, Erler A, Gioli B, Hamdi K, Hutjes R, Kosvancova M, Meroni M, Miglietta F, Moersch A. 2010. Remote sensing of sun-induced fluorescence to improve modeling of diurnal courses of gross primary production (GPP). *Global Change Biology* 16(1): 171-186. *

Damm A., Erler André, Hillen Walter, Meroni Michele, Schaepman Michael E., Verhoef Wout, Rascher Uwe (2011). Modeling the impact of spectral sensor configurations on the FLD retrieval accuracy of sun-induced chlorophyll fluorescence, *Remote Sensing of Environment*, Volume 115, Issue 8, Pages 1882-1892.

Damm A., Guanter L., Laurent V.C.E., Schaepman M.E., Schickling A., Rascher, U. (2014). FLD-based retrieval of sun-induced chlorophyll fluorescence from medium spectral resolution airborne spectroscopy data, *Remote Sensing of Environment*, Volume 147, Pages 256-266.

Damm, A., Guanter, L., Paul-Limoges, E., Van der Tol, C., Hueni, A., Buchmann, N., Eugster, W., Ammann, C. & Schaepman, M. E. (2015). Far-red sun-induced chlorophyll fluorescence shows ecosystem-specific relationships to gross primary production: An assessment based on observational and modeling approaches. *Remote Sensing of Environment*, 166, 91-105. *

Drusch, M., Del Bello, U., Carlier, S., Colin, O., Fernandez, V., Gascon, F., Hoersch, B., Isola, C., Laberinti, P., Martimort, P. & Meygret, A. (2012). Sentinel-2: ESA's optical high-resolution mission for GMES operational services. *Remote sensing of Environment*, 120, 25-36. *

Drusch M. et al. (2017) The FLuorescence EXplorer mission concept - ESA's Earth Explorer 8. *IEEE Transactions on Geoscience and Remote Sensing*, 55, 1273-1284, doi: 10.1109/TGRS.2016.2621820. *

El-Madany, T. S., Reichstein, M., Pérez-Priego, O., Carrara, A., Moreno, G., Pilar Martín, M., Pacheco-Labrador, J., Wohlfahrt, G., Nieto, H., Weber, U., Kolle, O., Yunpeng, L., Carvalhais, N., Migliavacca, M. (2018). Drivers of spatio-temporal variability of carbon dioxide and energy fluxes in a mediterranean savanna ecosystem. *Agricultural and Forest Meteorology*, 262, 258-278. doi:10.1016/j.agrformet.2018.07.010.

Frankenberg C, Fisher JB, Worden J et al. (2011) New global observations of the terrestrial carbon cycle from GOSAT: patterns of plant fluorescence with gross primary productivity. *Geophysical Research Letters*, 38, L17706. *

Gamon, J. A., Penuelas, J., & Field, C. B. (1992). A narrow-waveband spectral index that tracks diurnal changes in photosynthetic efficiency. *Remote Sensing of environment*, 41(1), 35-44. *

Gamon, John A., Huemmrich, K. Fred, Wong, Christopher Y. S., Ensminger, Ingo, Garrity, Steven, Hollinger, David Y., Noormets, Asko, Peñuelas, Josep (2016). Photosynthetic phenology of evergreen conifers, *Proceedings of the National Academy of Sciences* Nov 2016, 113 (46) 13087-13092. *

Graf A (2017) Gap-filling meteorological variables with Empirical Orthogonal Functions. EGU 2017 General Assembly, Vienna (Austria), 23 Apr 2017 - 28 Apr 2017, URL <https://user.fz-juelich.de/record/829701>, [Accessed 25 January 2019]. *

Guanter L, Frankenberg C, Dudhia A et al. (2012) Retrieval and global assessment of terrestrial chlorophyll fluorescence from GOSAT space measurements. *Remote Sensing of Environment*, 121, 236-251. *

Guanter L, Zhang YG, Jung M, Joiner J, Voigt M, Berry JA, Frankenberg C, Huete AR, Zarco-Tejada P, Lee JE, et al. 2014. Global and time-resolved monitoring of crop photosynthesis with chlorophyll

	Doc.: Photosynthesis report Version1		
	Date: 27.11.2019	Issue: 2	Revision: 1
	Ref.: ESA Contract No. ESA RFP/3-15506/18/NL/NF		Page: 66 / 69

fluorescence. Proceedings of the National Academy of Sciences of the United States of America 111(14): E1327-E1333. *

Huete, A., Didan, K., Miura, T., Rodriguez, E. P., Gao, X., & Ferreira, L. G. (2002). Overview of the radiometric and biophysical performance of the MODIS vegetation indices. *Remote sensing of environment*, 83(1-2), 195-213. *

Kraft, S., Del Bello, U., Harnisch, B., Bouvet, M., Drusch, M., & Bézy, J. L. (2017, November). Fluorescence imaging spectrometer concepts for the earth explorer mission candidate FLEX. In *International Conference on Space Optics—ICSO 2012* (Vol. 10564, p. 105641W). International Society for Optics and Photonics. *

Joiner J, Yoshida Y, Vasilkov AP, Yoshida Y, Corp LA, Middleton EM (2011) First observations of global and seasonal terrestrial chlorophyll fluorescence from space. *Biogeosciences*, 8, 637–651. *

Joiner, J., Yoshida, Y., Zhang, Y., Duveiller, G., Jung, M., Lyapustin, A., Wang, Y. and Tucker C.J. (2018). Estimation of Terrestrial Global Gross Primary Production (GPP) with Satellite Data-Driven Models and Eddy Covariance Flux Data. *Remote Sensing*, 10, 1346*

Lasslop G, Reichstein M, Papale D, Richardson AD, Arneth A, Barr A, Stoy P, Wohlfahrt G (2010) Separation of net ecosystem exchange into assimilation and respiration using a light response curve approach: critical issues and global evaluation. *Global Change Biology* 16(1):187–208. *

Lichtenthaler (1987) Chlorophylls and carotenoids – pigments of photosynthetic biomembranes. In *Methods in Enzymology* Eds SP Colowick and NO Kaplan) pp350-382. (Academic Press: Sydney). *

Lichtenthaler, H.K. and Buschmann, C. (2001) *Current protocols in Food and Analytical Chemistry*. F4.3.8-F4.2.4 *

Mauder, M., & Foken, T. (2011). Documentation and instruction manual of the eddy-covariance software package TK3. *

Mauder, M., Cuntz, M., Drüe, C., Graf, A., Rebmann, C., Schmid, H. P., Schmidt, M. & Steinbrecher, R. (2013). A strategy for quality and uncertainty assessment of long-term eddy-covariance measurements. *Agricultural and Forest Meteorology*, 169, 122-135. *

Mazzoni, M., Meroni, M., Fortunato, C., Colombo, R., & Verhoef, W. (2012). Retrieval of maize canopy fluorescence and reflectance by spectral fitting in the O2–A absorption band. *Remote sensing of environment*, 124, 72-82. *

Meroni, M., Rossini, M., Guanter, L., Alonso, L., Rascher, U., Colombo, R., & Moreno, J. (2009). Remote sensing of solar-induced chlorophyll fluorescence: Review of methods and applications. *Remote Sensing of Environment*, 113(10), 2037-2051. *

Meroni, M., Busetto, L., Colombo, R., Guanter, L., Moreno, J., & Verhoef, W. (2010). Performance of spectral fitting methods for vegetation fluorescence quantification. *Remote Sensing of Environment*, 114(2), 363-374. *

Migliavacca, M. , Perez-Priego, O. , Rossini, M. , El-Madany, T. S., Moreno, G. , van der Tol, C. , Rascher, U. , Berninger, A. , Bessenbacher, V. , Burkart, A. , Carrara, A. , Fava, F. , Guan, J. , Hammer, T. W., Henkel, K. , Juarez-Alcalde, E. , Julitta, T. , Kolle, O. , Martín, M. P., Musavi, T. , Pacheco-Labrador, J. , Pérez-Burgueño, A. , Wutzler, T. , Zaehle, S. and Reichstein, M. (2017), Plant functional traits and canopy structure control the relationship between photosynthetic CO₂ uptake and far-red sun-induced

	Doc.: Photosynthesis report Version1		
	Date: 27.11.2019	Issue: 2	Revision: 1
	Ref.: ESA Contract No. ESA RFP/3-15506/18/NL/NF		Page: 67 / 69

fluorescence in a Mediterranean grassland under different nutrient availability. *New Phytol*, 214: 1078-1091.

Ney, P., & Graf, A. (2018). High-resolution vertical profile measurements for carbon dioxide and water vapour concentrations within and above crop canopies. *Boundary-layer meteorology*, 166(3), 449-473.

Perez-Priego, O., Guan, J., Rossini, M., Fava, F., Wutzler, T., Moreno, G. and Carvalhais, N. and Carrara, A. and Kolle, O. and Julitta, T. and Schrupf, M. and Reichstein, M. and Migliavacca, M. (2015). Sun-induced Chlorophyll fluorescence and PRI improve remote sensing GPP estimates under varying nutrient availability in a typical Mediterranean savanna ecosystem. *Biogeosciences Discussions*, 12(14).

Pinto, F., Damm, A., Schickling, A., Panigada, C., Cogliati, S., Müller-Linow, M., Balvora, A. and Rascher, U., 2016. Sun-induced chlorophyll fluorescence from high-resolution imaging spectroscopy data to quantify spatio-temporal patterns of photosynthetic function in crop canopies. *Plant, cell & environment*, 39(7), pp.1500-1512.

Räsch, Anna & Muller, Onno & Pieruschka, Roland & Rascher, Uwe. (2014). Field Observations with Laser-Induced Fluorescence Transient (LIFT) Method in Barley and Sugar Beet. *Agriculture*. 4. 159-169. 10.3390/agriculture4020159.

Rascher U, Alonso L, Burkart A, Cilia C, Cogliati S, Colombo R, Damm A, Drusch M, Guanter L, Hanus J, Hyvärinen T, Julitta T, Jussila J, Kataja K, Kokkalis P, Kraft S, Kraska T, Matveeva M, Moreno J, Muller O, Panigada C, Piki M, Pinto F, Prey L, Pude R, Rossini M, Schickling A, Schurr U, Schüttemeyer D, Verrelst J, Zemek F., (2015). Sun-induced fluorescence - a new probe of photosynthesis: First maps from the imaging spectrometer HyPlant. *Glob Chang Biol*. 21(12) 4673-4684. doi:10.1111/gcb.13017. PMID: 26146813.*

REddyProc Team (2014) REddyProc: Data processing and plotting utilities of (half-) hourly eddy covariance measurements. R package version 1.1.3. URL <https://www.bgc-jena.mpg.de/bgi/index.php/Services/REddyProcWebRPackage>, [Accessed 25 January 2019].*

Reichstein, M., Falge, E., Baldocchi, D., Papale, D., Aubinet, M., Berbigier, P., ... & Grünwald, T. (2005). On the separation of net ecosystem exchange into assimilation and ecosystem respiration: review and improved algorithm. *Global change biology*, 11(9), 1424-1439.

Schickling, A., Matveeva, M., Damm, A., Schween, J., Wahner, A., Graf, A., Crewell, Susanne & Rascher, U. (2016). Combining sun-induced chlorophyll fluorescence and photochemical reflectance index improves diurnal modeling of gross primary productivity. *Remote Sensing*, 8(7), 574.

Sellers, P. J. (1987). Canopy reflectance, photosynthesis, and transpiration, II. The role of biophysics in the linearity of their interdependence. *Remote sensing of Environment*, 21(2), 143-183.*

Shan N, Ju W, Migliavacca M, Martini D, Guanter L, Chen J, Goulas Y, Zhang Y. 2019. Modeling canopy conductance and transpiration from solar-induced chlorophyll fluorescence. *Agricultural and Forest Meteorology* 268: 189-201.*

Simmer, C., I. Thiele-Eich, M. Masbou, W. Amelung, H. Bogen, S. Crewell, B. Diekkrüger, F. Ewert, H. Hendricks Franssen, J.A. Huisman, A. Kemna, N. Klitzsch, S. Kollet, M. Langensiepen, U. Löhnert, A.S. Rahman, U. Rascher, K. Schneider, J. Schween, Y. Shao, P. Shrestha, M. Stiebler, M. Sulis, J. Vanderborght, H. Vereecken, J. van der Kruk, G. Waldhoff, and T. Zerenner (2015). Monitoring and Modeling the Terrestrial System from Pores to Catchments: The Transregional Collaborative Research

	Doc.: Photosynthesis report Version1		
	Date: 27.11.2019	Issue: 2	Revision: 1
	Ref.: ESA Contract No. ESA RFP/3-15506/18/NL/NF		Page: 68 / 69

Center on Patterns in the Soil–Vegetation–Atmosphere System. *Bull. Amer. Meteor. Soc.*, 96, 1765–1787.*

Sotomayor, A. I. T. (2002, February). A spatial analysis of different forest cover types using GIS and Remote sensing techniques. ITC.*

Springer, K.R., Wang, R. and Gamon, J.A. (2017). Parallel Seasonal Patterns of Photosynthesis, fluorescence, and Reflectance Indices in Boreal Trees. *Remote Sensing* 9, 691*

Verhoef, W., & Bach, H. (2003). Simulation of hyperspectral and directional radiance images using coupled biophysical and atmospheric radiative transfer models. *Remote sensing of environment*, 87(1), 23-41.*

Verstraete, M. M., & Pinty, B. (1996). Designing optimal spectral indexes for remote sensing applications. *IEEE Transactions on Geoscience and Remote Sensing*, 34(5), 1254-1265.*

Vilà-Guerau de Arellano J. et al. (2015). Atmospheric boundary layer: integrating air chemistry and land interactions. Cambridge University Press.

Wieneke, S., Ahrends, H., Damm, A., Pinto, F., Stadler, A., Rossini, M., & Rascher, U. (2016). Airborne based spectroscopy of red and far-red sun-induced chlorophyll fluorescence: Implications for improved estimates of gross primary productivity. *Remote Sensing of Environment*, 184, 654-667.

	Doc.: Photosynthesis report Version1		
	Date: 27.11.2019	Issue: 2	Revision: 1
	Ref.: ESA Contract No. ESA RFP/3-15506/18/NL/NF		Page: 69 / 69

6 Acknowledgement

This work is based on results from John Gamon, Mirco Migliavacca, David Martini, Uwe Rascher and Vera Krieger, Patrizia Ney, Marius Schmidt, Alexander Graf among many others.